Aberystwyth University

Paraglacial adjustment of alluvial fans to the last deglaciation in the Snežnik Mountain, Dinaric karst (Slovenia)

Žebre, Manja; Jež, Jernej; Mechernich, Silke; Mušič, Branko; Horn, Barbara; Jamšek Rupnik, Petra

1 **Paraglacial adjustment of alluvial fans to the last deglaciation in the Snežnik**
2 **Mountain, Dinaric karst (Slovenia)**

3 Manja Žebre[a] [*], Jernej Jež[a], Silke Mechernich[b], Branko Mušič[c, d], Barbara Horn[c],
4 Petra Jamšek Rupnik[a]

5 [a] Geological Survey of Slovenia, Dimičeva ulica 14, 1000 Ljubljana, Slovenia
6 [b] Institute for Geology and Mineralogy, University of Cologne, Zuelpicherstr. 49b,
7 50937 Köln, Germany
8 [c] GEARH d.o.o., Radvanjska 13, 2000 Maribor, Slovenia
9 [d] University of Ljubljana, Department of Archaeology, Aškerčeva 2, 1000 Ljubljana,
10 Slovenia

11 Corresponding author. E-mail address: manjazebre@gmail.com, maz24@aber.ac.uk (M.
12 Žebre).

*Present address: Department of Geography & Earth Sciences, Aberystwyth University,
Llandinam Building, Penglais Campus, SY23 3DB, Aberystwyth, United Kingdom*

13 **Abstract**

14 Glaciokarst depressions are major glacigenic depocenters in the Dinaric mountain

15 karst areas and often store important information about the timing and nature of

16 glacial processes and paraglacial sediment reworking. This study focuses on

17 Praprotna draga, which is one of the largest glaciokarst depressions in the Snežnik

18 Mountain (Dinaric karst), with an area of ~3.4 km^2 and a maximum depth of 140 m.

19 The western slopes of the depression are characterized by undulated moraine

20 morphology and alluvial fans are filling its entire floor. We present the results on the

21 thickness, origin and age of the sediment infill using a complementary

22 geomorphological, sedimentological, geophysical and dating approach. Distribution

23 of moraines point to two glacial advances that were associated with two main alluvial

24 fan aggradation phases recognised using the electrical resistivity tomography

25 measurements. The youngest alluvial deposits were sampled for cosmogenic ^{36}Cl

26 analysis using amalgamated carbonate pebbles. The depth profile of ^{36}Cl

27 concentrations suggests an age of 12.3 ± 1.7 ka when assuming a likely denudation

28 rate of 20 mm ka^{-1}. Since the existence of the Younger Dryas glaciers in the study

29 area is climatically difficult to explain, we tentatively propose that the youngest

30 alluvial deposition in Praprotna draga took place after the glacier retreat during the

31 paraglacial period. Our findings suggest that the time window of paraglacial

32 adjustment in the Snežnik Mountain was brief and likely conditioned by quick

33 recolonization with vegetation and inefficient surface runoff on deglaciated karst

34 terrain.

35 **Keywords**: Dinaric karst, Electrical Resistivity Tomography, Cosmogenic dating,

36 Younger Dryas, Paraglacial

1. Introduction

Little information is currently available about the deglaciation of Dinaric karst and the Balkan Peninsula, and even less is known on the nature of paraglacial sedimentation in this same area. Although Dinaric karst is known for widespread and well-developed karst phenomena (Cvijić, 1893) and is referred to as *locus typicus* for the karst worldwide, it is also of interest because its mountainous parts experienced glaciations during the Quaternary cold stage climates, resulting in a glaciokarst type of landscape (Smart, 2004; Žebre and Stepišnik, 2015). The last deglaciation of the Dinaric mountain karst areas is chronologically still poorly constrained. For example, the Younger Dryas deglaciation has been dated in the Orjen Mountain (Montenegro) (Hughes et al., 2010), Šar Planina (Kuhlemann et al., 2009) and Galičica mountains (Ribolini et al., 2011; Gromig et al., 2018) (both located in FYROM), and Mount Chelmos (Pope et al., 2015) and Mount Olympus (Styllas et al., 2018) (both located in Greece), whereas the Oldest Dryas deglaciation has been recorded in the Mount Pelister (FYROM) (Ribolini et al., 2018). However, data on the last deglaciation elsewhere in the Balkans are generally missing (e.g., Milivojević et al., 2008; Žebre and Stepišnik, 2014).

On the other hand, the glacial geomorphology in Dinaric karst is relatively well-studied (e.g., Milivojević et al., 2008; Žebre and Stepišnik, 2014; Krklec et al., 2015). Closed depressions, which are characteristic features for Dinaric karst (Mihevc and Prelovšek, 2010), are also present in other karst landscapes that were once glaciated, such as the Julian Alps (Colucci, 2016) and Dachstein Mountains (Veress, 2017) in the European Alps, Picos de Europa (Smart, 1986) and Taurus Mountains (Sarıkaya and Çiner, 2017). These so-called "glaciokarst depressions" (Ćalić, 2011; Veress, 2017), particularly those located at the edge of terminating glaciers and thus

62   experiencing key aggradation phases, are major depocenters for glacigenic deposits

63   in karst areas (Adamson et al., 2014; Žebre et al., 2016). As a result, glaciokarst

64   depressions often host valuable proxy-data, which are important sources of

65   information for palaeoenvironmental and palaeolandscape studies.

66   Glaciers produce vast amounts of sediments that are later transported, deposited

67   and reworked by fluvial streams, but it is not always clear whether these sediments

68   were deposited directly by meltwaters, or rather at the end of, or after glacier retreat.

69   Fluvial aggradation in glacial catchments primarily takes place during phases of

70   glacial advance, when glaciers are eroding and exporting sediment downstream, and

71   also for the period of paraglacial adjustment, when glacially conditioned sediments

72   are being reworked (Cordier et al., 2017). Paraglacial processes tend to adjust the

73   relief to non-glacial conditions, thus generating a transitional landscape (Slaymaker,

74   2009), which starts at deglaciation and terminates when sediment yields drop to rates

75   which are typical of unglaciated catchments (Ballantyne, 2002; Mercier, 2008). The

76   duration and intensity of paraglacial adjustment depends on the amount of sediment

77   deposited at palaeo-glacier margins, the rate of slope erosion processes and

78   environmental conditions such as post-glacial climate, timing of vegetation change,

79   catchment size and morphology (Church and Slaymaker, 1989; Harbor and

80   Warburton, 1993; Ballantyne, 2003; Cordier et al., 2017). Although it has been

81   suggested that the paraglacial period in the karst areas of the Balkan Peninsula was

82   short-lived due to quick recolonization with vegetation and subsequent stabilization of

83   deglaciated terrain (Adamson et al., 2014; Woodward et al., 2014), there are still

84   several uncertainties about the timing of paraglacial adjustment and the nature of

85   sediment reworking in this area. These are the key for understanding the evolution of

86   deglaciated glaciokarst landscapes. Therefore, this paper aims at unravelling and

87 better constraining the timing of paraglacial sedimentation in the Snežnik Mountain

88 (Dinaric karst, Slovenia) (Fig. 1) by studying the sediment infill of the Praprotna draga

89 karst depression using geomorphological mapping, sediment facies analysis,

90 electrical resistivity tomography measurements and cosmogenic ^{36}Cl nuclide

91 exposure dating. The interpretation of the results from Praprotna draga is supported

92 by the geomorphological map of the entire Snežnik area (Žebre and Stepišnik, 2016).

2. Regional setting

94 Snežnik Mountain is located in the southern part of Slovenia, close to the national

95 border with Croatia and represents a NW continuation of the Gorski Kotar

96 mountainous area (Fig. 1a). The highest altitude in this area is Veliki Snežnik peak

97 (1796 m a.s.l.).
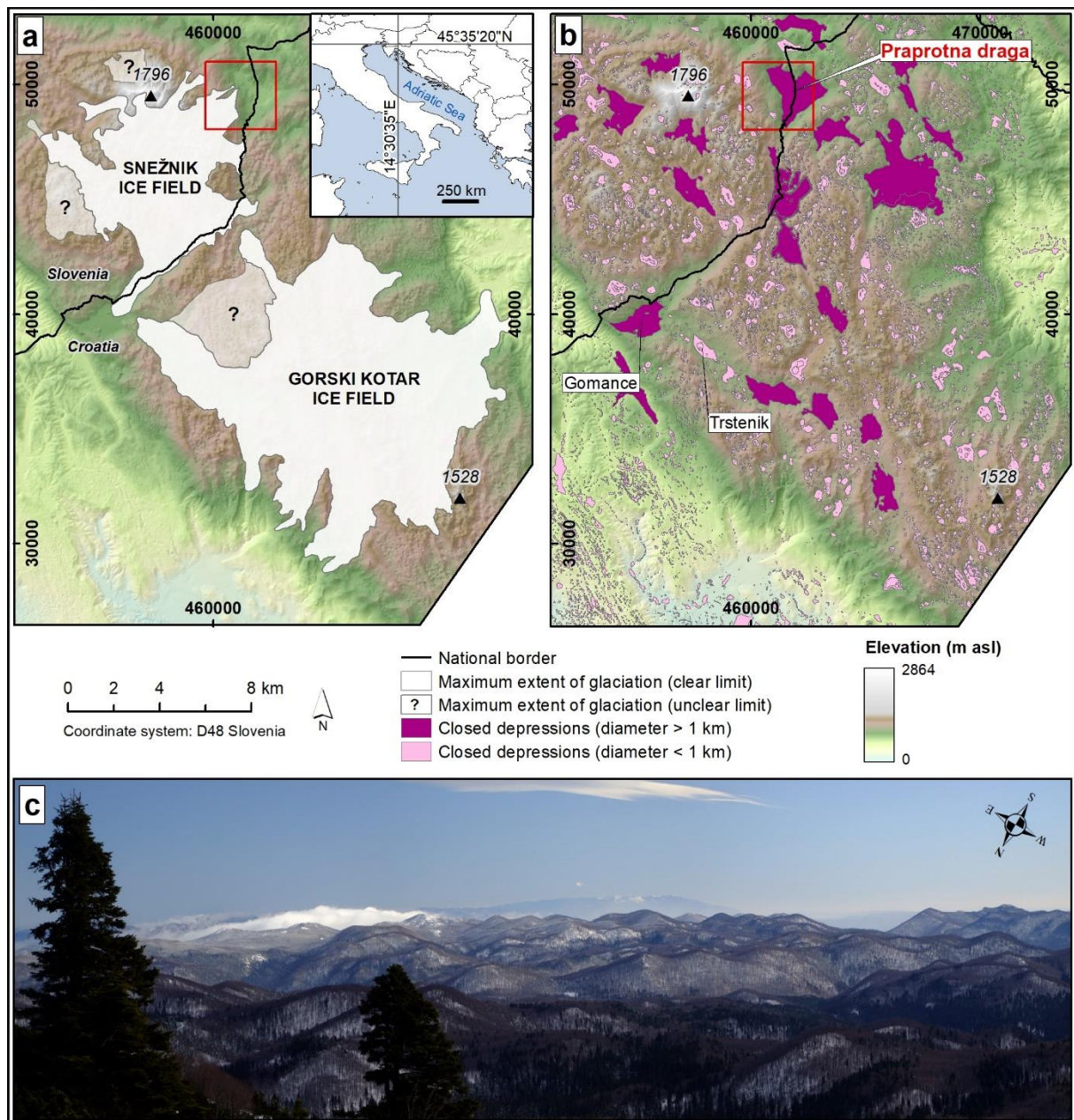
Fig. 1: (a) The maximum recorded phase of glaciation in the Snežnik and NW Gorski kotar area (modified after Žebre and Stepišnik (2016)). (b) Distribution of closed depressions in the Snežnik and NW Gorski Kotar, extracted from a 10 m DEM using the algorithm designed by Grlj and Grigillo (2014). The Praprotna draga study area in (a) and (b) is marked with a red square. (c) Photo of the Snežnik area southeast of the highest peak, where the high grade of karstification is visible in the widespread dolines (photo courtesy of Renato R. Colucci).

2.1. Geology, geomorphology and former chronological data

The Snežnik area belongs to the northwestern part of the External Dinarides, a SW-verging fold-and-trust belt (e.g., Placer, 1998; Vrabec and Fodor, 2006). Due to intense tectonic shortening during the Cenozoic, the area is divided into several thrusts (Placer, 1998). Snežnik and Gorski Kotar represent a part of the Snežnik thrust, a vast tectonic unit that covers a large part of SW Slovenia, predominantly composed of Mesozoic carbonates. The Veliki Snežnik area is mainly composed of bedded to thin bedded Upper Jurassic to Lower Cretaceous limestone, while locally bedded dolomite and limestone-dolomite breccia are also common. Fold and thrust structure is dissected by NW-SE-striking dextral faults and associated NNW-SSE-striking faults belonging to the Dinaric Fault System and representing the neotectonic structural style visible in mountain morphology (e.g., Vrabec and Fodor, 2006; Moulin et al., 2016). Limestone in the Snežnik area is subjected to a rapid karstification resulting in many karstic features (e.g., vertical shafts, sinkholes).

Quaternary sediments have been documented already during geological investigations in the late 1950s and 1970s (Šifrer, 1959; Šikić et al., 1972). These sedimentary bodies of glacigenic origin stand out from the surrounding karstic areas (Figs. 1b and 1c), especially due to their characteristic morphological features. No rock glacier remnants or macro periglacial features exist in the area according to past studies (Colucci et al., 2016; Oliva et al., 2018). The majority of glacial deposits in the form of up to ~50 m high lateral and frontal moraines are distributed on the southern and eastern slopes at elevations between 900 and 1200 m a.s.l. They reach the lowest altitudes in the Gomance karst depression on the southern slopes of Snežnik (900 m a.s.l., Fig. 1b). The western part of Snežnik is dominated by hummocky moraines, reaching down to 1060 m a.s.l. Moraines on the northeastern side are

131 mainly located around the Praprotna draga karst depression, while surprisingly no

132 glacial evidence was identified north of the highest peak (Žebre and Stepišnik, 2016).

133 Typical glacial erosional forms are not common for the Snežnik area. Small glacial

134 erosional features such as striae and chattermarks are almost entirely absent, which

135 is likely a result of high dissolution rates. Other characteristic erosional forms for

136 mountain glaciation, such as cirques and U-shaped valleys, are rare as well (Žebre

137 and Stepišnik, 2016). On the other hand, the area is dissected by glaciokarst

138 depressions, which are most likely formed primarily by karst processes and

139 subglacial erosion (e.g., Smart, 1986; Žebre and Stepišnik, 2015).

140 The largest and the deepest depressions here reach more than 2 km in diameter and

141 140 m in depth, having floors filled with glacigenic deposits. In the Gomance karst

142 depression (Fig. 1b) on the southern flanks of the Snežnik massif, a bone found in

143 outwash deposits was dated to 18.7 ±1.0 cal ka BP (recalculated with IntCal13

144 calibration; Reimer et al., 2013) (Marjanac et al., 2001). This age points to an

145 outwash event during the largest recognized extent of the Snežnik and the nearby

146 Gorski Kotar ice fields, which is estimated to at least 140 km^2 during the Last Glacial

147 Maximum (LGM) (Žebre et al., 2016) (Fig. 1a). In the Trstenik karst depression (950

148 m a.s.l.) (Fig. 1b), located less than 2 km east of Gomance, pollen analyses indicate

149 the presence of Late-glacial lacustrine deposits at a depth of ~2 m (Šercelj, 1971). In

150 contrast to Gomance, where the floor is predominantly filled with outwash and till

151 deposits, Trstenik mainly hosts peat and gyttja underlain by proglacial lacustrine

152 deposits.

153 *2.2.   Climate and vegetation*

154 Due to the proximity of Snežnik to the cyclogenetic area of the northern Adriatic Sea

155 and the Genova Bay, the present climate in the study area is characterized by high

156 precipitation (Isotta et al., 2014), intensified by the orographic effect (Zaninović et al.,

157 2008). Mean annual precipitation (MAP) for the period 1931–1960 at Gomance (937

158 m a.s.l.) was 2792 mm and mean annual air temperature was 6.6 °C (Pučnik, 1980),

159 but the highest elevations currently receive a MAP of >3500 mm and the mean

160 annual air temperature there was estimated to 2–3 °C (Zaninović et al., 2008). The

161 mean seasonal snow cover duration for the period 1961/62-1990/1991 is 100–150

162 days and mean seasonal fresh snow accumulation for the same period is 280–420

163 cm (http://meteo.arso.gov.si/met/en/climate/maps/).

164 The dominant vegetation community in the Snežnik high karst plateau consists of

165 Dinaric silver fir—European beech forest (*Omphalodo-Fagetum*), with European

166 beech (*Fagus sylvatica*), silver fir (*Abies alba*), and Norway spruce (*Picea abies*) as

167 the dominant tree species (Surina and Wraber, 2005; Kobal et al., 2015). Spruce

168 forest occurs only azonally and is generally confined to dolines as a result of

169 temperature inversion. The tree line is situated at ~1500 m a.s.l. and is marked by

170 presence of subalpine beech stands (*Polysticho lonchitis-Fagetum*) (Surina and

171 Wraber, 2005; Komac et al., 2012).

172 **3. Methods**

173 In this paper, we combine various methods including high-resolution

174 geomorphological mapping, sediment facies analyses, cosmogenic nuclide dating

175 and geophysical measurements to study the sedimentological composition, geometry

176 and age of deposits filling the Praprotna draga karst depression in the Snežnik

177 Mountain.

3.1. Geomorphological mapping

The glacial geomorphological map of Praprotna draga (Fig. 2a) was obtained by updating the previously published geomorphological map of glaciokarst features in Snežnik and NW Gorski Kotar area by Žebre and Stepišnik (2016). We mapped the geomorphological features in the Praprotna draga karst depression by means of field mapping, supported by 1:10.000 and 1:25.000 topographic maps and 1-m resolution digital elevation model (DEM), derived from LiDAR data (Ministry of the Environment and Spatial Planning, Slovenian Environment Agency) with relative horizontal and vertical accuracies of 0.30 and 0.15 m, respectively. With the analysis of LiDAR data we updated the previously published geomorphological map, which was based on topographic maps. The LiDAR data is most suitable for geomorphological mapping due to dense forest cover and in parts dense undergrowth. A LiDAR DEM was processed to produce several maps (shaded relief, topographic curves with 1 m equidistance, slope degree map, slope aspect map) that served as a basis for detailed mapping of individual alluvial fans and moraines.

3.2. Sedimentological characterization

In the area of the mapped alluvial fans and moraine ridges we logged in detail seven up to 2.7 m deep outcrops (3 road cuttings and 4 trenches) (Figs. 3 and 4). We identified key sediment parameters such as sedimentary structures, colour, clast lithology, size, distribution and roundness by using standard field techniques. Lithofacies codes from Evans and Benn (2004) were used for sediment description, which was based on macroscopic observations. We used these data as ancillary information for the geomorphological interpretation of sediment depositional environment and establishing a relationship between electrical resistivity tomography (ERT) data and sedimentary bodies.

3.3. Cosmogenic ^{36}Cl nuclide exposure dating

Given the lack of suitable dating material for radiocarbon (absence of organic material within the deposits) and luminescence (lack of quartz and feldspar) methods, we estimated the age of alluvial fans using cosmogenic exposure dating. This dating method is based on the formation of radionuclides due to the interaction of cosmic rays that occur at a calculatable rate. While in quartz-bearing lithologies cosmogenic radionuclide ^{10}Be is nowadays used almost routinely to constrain ages of late Quaternary landforms (Dunai, 2010; Schmidt et al., 2011; Ruszkiczay-Rüdiger et al., 2016b; Ribolini et al., 2018), the cosmogenic nuclide ^{36}Cl is the nuclide of choice for carbonate lithologies (Frankel et al., 2007; Gromig et al., 2018; Marrero et al., 2018; Mechernich et al., 2018; Styllas et al., 2018). When dating depositional surfaces such as debris flows or alluvial fans, it is necessary to take into account that cosmogenic nuclides are not only produced after formation of the respective surfaces, but also during erosion of the host rock and sedimentary transport of clasts. We obtained this pre-depositional nuclide component (i.e. inherited component) by using a depth profile (e.g., Hancock et al., 1999; Braucher et al., 2011; Schmidt et al., 2011; Rixhon et al., 2018).

3.3.1. Sampling strategy

We sampled one alluvial fan profile (PD-02; Figs. 2 and 3, Table 1) for cosmogenic ^{36}Cl depth profile analysis. Since the available limestone clasts are rather small (diameter of ~3–9 cm), the amount of material from individual clasts is too low for a precise measurement. Hence, limestone clasts within depth intervals of 5 cm were amalgamated to samples composed of 5–6 clasts (Table 2). All selected clasts were subangular to subrounded limestones, with a similar diameter of 3–9 cm. The amount of comparable clasts in a horizontal distance of ±1 m was scarce, hence no further

228   clasts were used for an amalgamation. Since bioturbation and denudation processes

229   likely changed the concentration of cosmogenic nuclides at the surface (Hein et al.,

230   2009), we took only subsurface samples.

Outcrop ID	Elevation (m a.s.l)	Latitude (N)	Longitude (E)
ME-01	1230	45°35'20.81"	14°29'0.68"
ME-02	1013	45°35'15.82"	14°29'43.87"
ME-03	995	45°35'30.66"	14°29'30.47"
PD-01	852	45°35'40.64"	14°29'34.73"
PD-02	837	45°35'48.29"	14°29'55.71"
PD-03	797	45°35'26.34"	14°30'0.47"
PD-06	782	45°35'25.67"	14°30'51.30"

231   Table 1. Elevations and coordinates of the studied outcrops.

Sample name	Depth interval (cm)	Amount of pebbles	Size of pebbles (cm)	Dissolved amount of sample (g)	Cl spike (*mg*)	Ca conc. ICP-OES (%)	Blank correction (%)	Stable Cl (µg/g)	^{36}Cl (10^5 atoms/g)	± ^{36}Cl (%)
CRN PD-02/ 25-30	25-30	5	5-8	20.1379	1.4848	37.7%	0.41%	47.3 ± 1.9	5.11 ± 0.23	4.4%
CRN PD-02/ 75-80	75-80	5	3-6	20.4658	1.4892	38.3%	0.66%	48.5 ± 2.0	3.14 ± 0.16	5.0%
CRN PD-02/ 105-110	105-110	6	4-9	19.7269	1.4859	38.7%	0.82%	49.7 ± 2.0	2.61 ± 0.11	4.4%
CRN PD-02/ 215-220	215-220	5	3-6	29.6144	1.4832	37.3%	0.48%	49.6 ± 2.2	2.95 ± 0.12	4.1%

232   Table 2: Location of the cosmogenic samples of site PD-02 within the depth profile

233   and their major chemical concentrations relevant for the ^{36}Cl nuclide exposure dating.

234   The full relevant chemical composition is presented in Table S1. All sampled

235   individual clasts were composed of limestone. Reported uncertainties are within the

236   1σ range.

237   *3.3.2. Sample preparation and measurements*

238   The samples were mechanically cleaned, crushed and sieved to the 250-500 µm size

239   fractions at the Geological Survey of Slovenia. The chemical treatment was

240   performed at the University of Edinburgh (UK) using the protocol of Marrero et al.

241   (2018). The concentration of ^{36}Cl and natural chlorine was measured via accelerator

242   mass spectrometry (AMS) at the Cologne AMS facility (Tables 1 and S2). Within the

243   same preparation and measurement cycle as the samples of PD-02, nine aliquots of

244   the carbonatic interlaboratory calibration material CoCal-N (Mechernich et al., 2019)

245   allow a direct quality control (Table S2). In order to calculate the specific production

246   rate of ^{36}Cl of the samples along the depth profile, an aliquot of each AMS-measured

247   fraction was analysed by ICP-OES at the University of Edinburgh. Additionally, major

248   and trace element contents of bulk non-leached sample material were measured at

249   Actlabs, Canada (Table S1).

250   *3.3.3. Determination of ^{36}Cl ages*

251   We computed the exposure age scenarios of the alluvial deposits by a depth profile

252   using the Excel spreadsheet of Schimmelpfennig et al. (2009). The following ^{36}Cl

253   production rates were integrated in the spreadsheet: 48.8 atoms ^{36}Cl (g Ca)$^{-1}$ a^{-1} for

254   the spallation of calcium at sea level and high latitude (Stone et al., 1996 with scaling

255   of Stone, 2000), spallation on K: 150 atoms ^{36}Cl (g K)$^{-1}$ a^{-1} (Marrero et al., 2016a),

256   spallation on Ti: 13 atoms ^{36}Cl (g Ti)$^{-1}$ a^{-1} (Fink et al., 2000), spallation on Fe: 1.9

257   atoms ^{36}Cl (g Fe)$^{-1}$ a^{-1} (Stone, 2005), 245 atoms g^{-1} a^{-1} for the slow negative muon

258   stopping rate (site-dependent value calculated from Marrero et al. 2016b), and 759 n

259   cm^{-2} a^{-1} for production from low-energy neutron absorption from ^{35}Cl (Marrero et al.,

260   2016a). For each sample, the resulting amounts of ^{36}Cl production by the major

261   mechanisms are shown in Table S2. Topographic shielding corrections as well as the

262   sample-specific attenuation length were determined using the CRONUS topographic

263   shielding calculator (https://hess.ess.washington.edu/).

264   For specific scenarios of denudation rates and soil densities, the most likely exposure

265   age scenarios and their corresponding pre-depositional ^{36}Cl concentrations were

266   iteratively determined based on ^{36}Cl concentrations at the different subsurface depths

267   of the samples (e.g., Frankel et al., 2007; Schmidt et al., 2011; Mechernich et al.,

268   2018) (Table 4).

269   *3.4. Electrical resistivity tomography (ERT)*

270   In most rocks (and sediments) electrical conduction is mostly the consequence of

271   pore fluids acting as electrolytes, with the actual mineral grains contributing very little

272   to the overall conductivity (and its reciprocal resistivity) of the rock (Reynolds,

273   1997).The electrical conductivity of rocks and soils is clearly dependent on the

274   amount of water in the medium, the conductivity of water and the way water is spread

275 (porosity, the degree of saturation, cementation factor, fracturing) (Kowalczyk et al.,

276 2014). Laboratory measurements of soil and sediment show high dependence of

277 resistivity on the sample's moisture content (degree of saturation) and porosity (e.g.,

278 Kowalczyk et al., 2014; Merritt et al., 2016). Hence, the different authors report

279 different resistivity ranges for similar sediment bodies and bedrock, respectively

280 (Table 3).

Lithology	Resistivity (Ωm)	Reference
Clay	up to 100	Ebraheem et al. (2013)
Clay	up to 50	Chambers et al. (2013)
Muddy sand	50–300	Pellicer and Gibson (2011), Chambers et al. (2013)
Gravelly muddy sand	50–400	Pellicer and Gibson (2011)
Gravelly sand	700–1200	Pellicer and Gibson (2011)
Sand and gravel	900	Chambers et al. (2013)
Sand and gravel	200–600	Chambers et al. (2011)
Gravel	300–1500	Beresnev, Hruby and Davis (2002)
Gravel	800–1500	Pellicer and Gibson (2011)
Saturated gravel	up to 150	Ebraheem et al. (2013)
Gravel (dry)	3000–6000	Ebraheem et al. (2013)
Fluvioglacial sand and gravel	700–1500	Chambers et al. (2011, 2013)
Fluvioglacial gravel, diamicton	100–1000	Pellicer et al. (2012)
Muddy diamicton	150–300	Pellicer and Gibson (2011)
Till	up to 1200	Dietrich and Krautblatter (2017)
Clayey till	~20	Chambers et al. (2011)
Limestone bedrock	1000–5000	Pellicer et al. (2012)
Limestone bedrock	1000–3000	Pellicer and Gibson (2011)
Limestone bedrock (dry)	up to 10000	Ebraheem et al. (2013)

281 Table 3. Published data on resistivity values of different lithologies.

282

283 To address our research objectives, we measured two 2-D ERT profiles in the

284 Praprotna draga site (Figs. 2a and 6). Profile a (94 m length) was measured

285 perpendicular to the direction of the moraine ridge in order to obtain the significant

286 resistivity values and estimate the thickness of glacial deposits. Profile b (635 m in

287 length) was measured in the longitudinal direction over the northernmost alluvial fan

288 that starts on the slope (917 m a.s.l.) and ends in the depression (835 m a.s.l.), in

289 order to determine the possible existence of other sedimentary bodies buried below

290 the alluvial deposits and to obtain the overall thickness and spatial distribution of

291 sediments. Profile b was not positioned in the straight line due to lush undergrowth,

292 but along the forest pathway. Dipole-dipole and Wenner-Schlumberger arrays with 2

293 m electrode spacing were applied in Profile a, and dipole-dipole array with 5 m

294 electrode spacing (roll-along technique) in Profile b. Two sections of the Profile b

295 were also measured with 2 m electrode spacing, b1 (0–158 m, Wenner-

296 Schlumberger array, roll-along technique) and b2 (dipole-dipole, 516–610 m) to

297 provide a better resolution for the upper 18 m of the subsurface. All measured

298 apparent resistivity pseudosections were inverted using the finite-element method

299 (Silvester and Ferrari, 1990), with a difference between the model response and the

300 observed data values reduced using the l1 norm smoothness-constrained Gauss-

301 Newton least-squares optimization method, where the absolute difference (or the first

302 power) between the measured and calculated apparent resistivity values is

303 minimized (Claerbout and Muir, 1973), known also as a blocky inversion method

304 (Loke et al., 2003). A small cut-off factor was applied on the robust model constrain.

305 The distribution of model cells is generated based on the sensitivity values (Jacobian

306 matrix) of the model cells, which takes into account the information contained in the

307 data set concerning the resistivity of the subsurface for a homogeneous earth model

308 and tries to ensure that the data sensitivity of any cell does not become too small

309 (Loke, 2013). Model refinement with a half width of one unit electrode spacing is

310 used in all models. Joint inversion (Athanasiou et al., 2007) with dipole-dipole and

311 Wenner-Schlumberger data sets was applied to the Profile a.

4.   Results

4.1.   Geomorphological and sedimentological characteristics

Praprotna draga is a large karst depression in the eastern part of Snežnik, which was modified by glacial and periglacial processes (Figs. 1b and 2a). We found that the area of the depression is 3.4 km^2 and the average diameter is ~ 2080 m. This 140 m deep depression has a minimum altitude of 780 m a.s.l. and its western slopes are characterized by undulated moraine morphology. Moraine ridges extend in the altitudinal range of 900-1290 m a.s.l. and are no more than 20 m high.
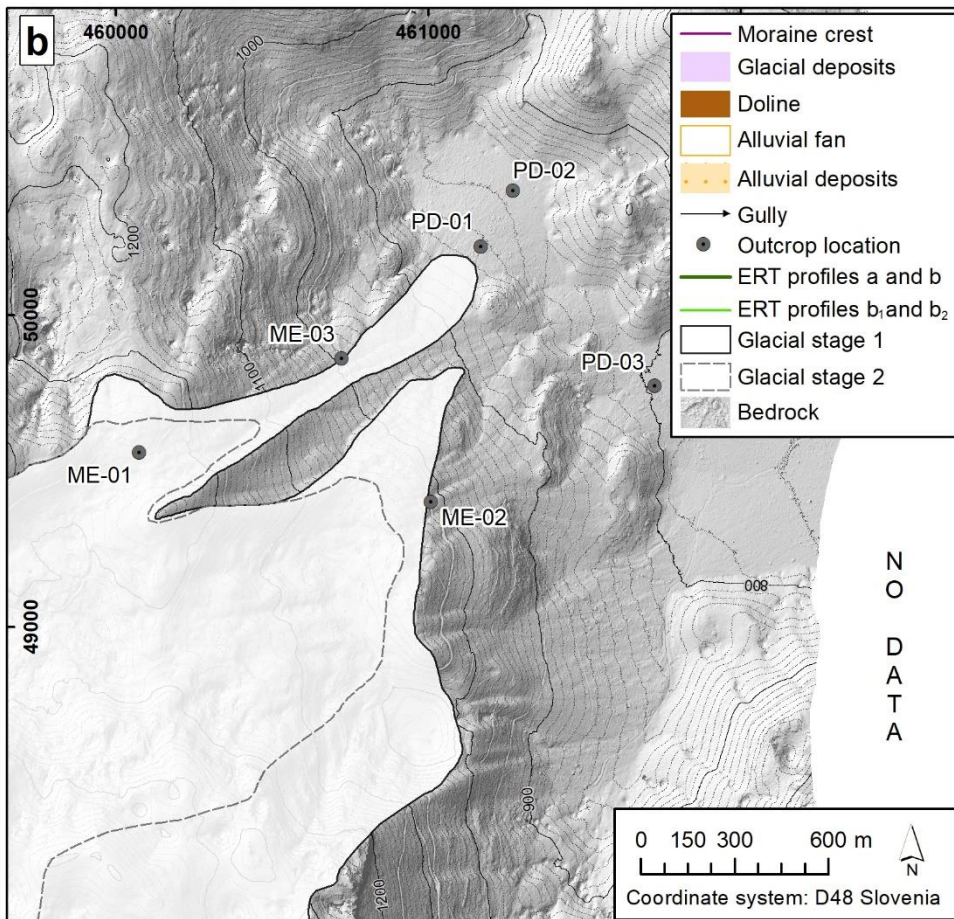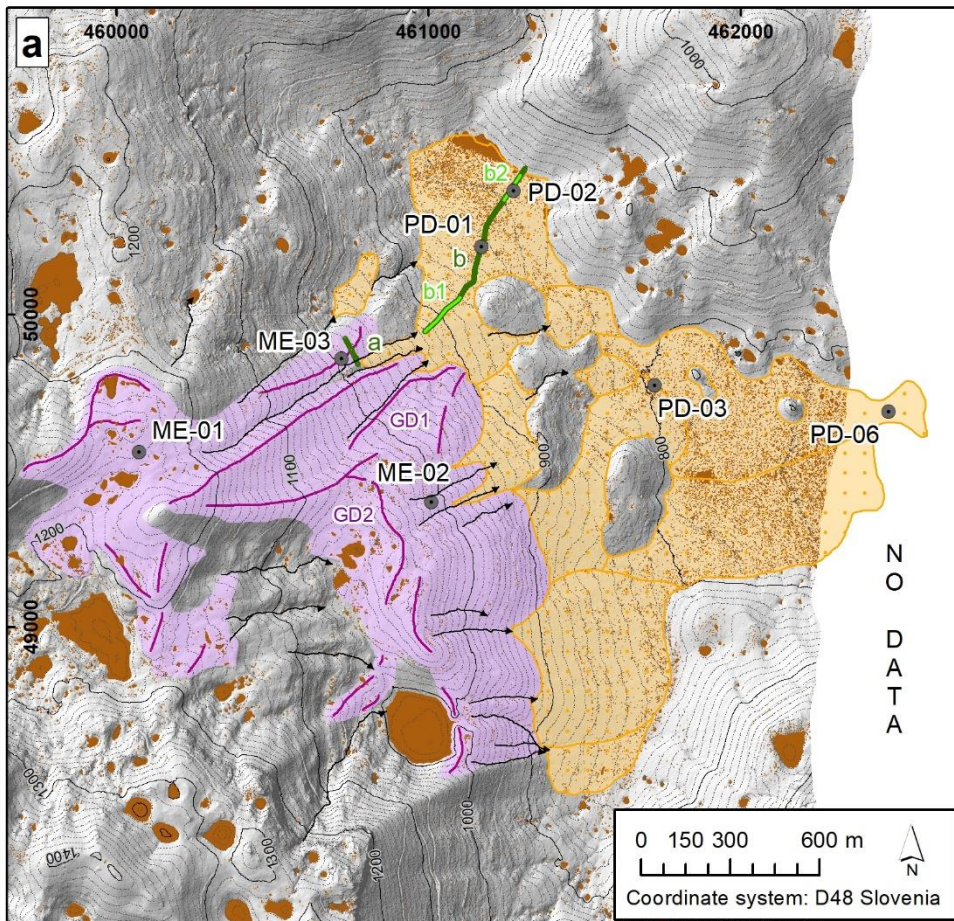
320

321 Fig. 2. (a) Glacial geomorphological map of Praprotna draga, including locations of

322 sediment logging and ERT profiles. Doline areas were extracted from a 1 m DEM

323 using the algorithm designed by Grlj and Grigillo (2014). GD1 and GD2 mark

324 stratigraphically older and younger moraines, respectively. (b) Proposed extent of

325 two glacial stages in the Praprotna draga depression, recognized on the basis of

326 geomorphological, sedimentological and geophysical evidence.

327 We found that the upper-laying moraines (ME-01; Fig. 2a, Table 1) consist of a

328 matrix-supported massive diamicton (Dmm) with subangular, polished and bullet-

329 shaped clasts. The deposit becomes more clast-supported towards lower elevations

330 and steeper slopes (ME-02 and ME-03; Table 1), where a matrix- to clast-supported

331 massive to roughly stratified diamicton (Dmm-Dcs) dominates the composition of

332 moraines. We observed a reduction in average and maximum clast size from 3–10

333 cm (max. 60 cm) in the ME-01 outcrop to 1–5 cm (max. 30 cm) in the ME-02 and

334 ME-03 outcrops. Moreover, the clast roundness is greater heading towards the lower

335 sections of moraines, where subangular to subrounded clasts prevail. Larger clasts

336 commonly show greater modification in roundness. The soil thickness passes from

337 15 to max. 30 cm (Fig. 3). We performed clast lithological analysis in the ME-01

338 outcrop with the aim to identify a general provenance of sedimentary facies. Grey to

339 dark-grey micritic laminated limestone of mudstone to wackestone textural types and

340 locally dolomitized limestone prevails, suggesting typical Lower Cretaceous

341 carbonate platform lithofacies. These are exposed in a wider area of the topmost

342 parts of the Snežnik Mountain, W and SW of Praprotna draga (Šikić et al., 1972).
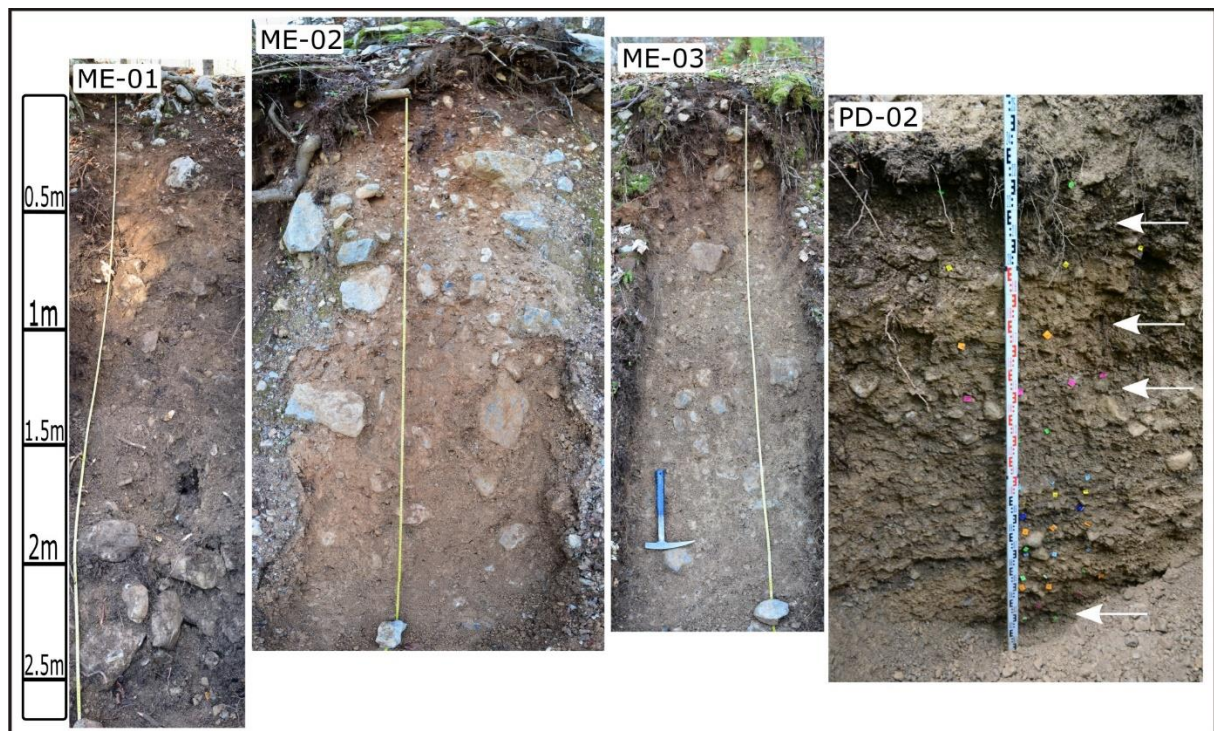
343

Fig. 3. Photos of till outcrops ME-01, ME-02, and ME-03, and the PD-02 sampling

site in alluvial deposits. Flags of different colours indicate sedimentary boundaries

within the profile PD-02. The sampled depth intervals are marked with white arrows.

For location of the outcrops see Fig. 2 and Table 1.

Fig. 4. Sedimentological logs of the trenches located in the alluvial fan. The [36]Cl

sampled locations in PD-02 are marked with red dotted line square. For location of

the trenches, see Fig. 2.

Below the moraines (>920 m a.s.l.), we mapped several alluvial fans that cover the

western slopes and the entire floor of the depression, while some bedrock ridges

crop out between them (Fig. 2). The southern fans are steeper in their proximal part

(15-30°) from the northern fans (10-20°). They all merge towards east, where the

mean gradient is 3-4°. Small dolines are present in the distal-most part of the fan

area and at the contact with the eastern bedrock (limestone) slopes of the Praprotna

draga depression. The formation of sufossion dolines in alluvial deposits indicates

active karst processes.

The alluvial fans consist of stratified, poorly to moderately sorted, sub-angular to

rounded gravels with occasional sand lenses (Fig. 4). The proximal fan zones (PD-

01; Table 1) are dominated by poorly sorted, moderately to well-rounded coarse-gravel facies consisting of massive to crudely bedded, clast-supported gravels (Gm), where gravel occupy between 70–90%, sand 0–15% and mud 0–30%. Towards the mid-fan zone (PD-02 and PD-03; Fig. 2a and Table 1) the gravel facies exhibit a marked downstream decline in the mean and maximum clast size, from 1–9 cm (max. 30 cm) to 0.2–6 cm (max. 5–15 cm). Poorly to moderately sorted, sub-angular to well rounded, massive to crudely horizontally bedded, clast supported gravels (Gm-Gh), where gravels occupy 70–95%, sand 0–30% and mud 0–15%, are interbedded with washed-out horizons and sparse sandy to silty lenses; lateral variations in facies type may occur due to the local channel network. The lower fan zone (PD-06; Fig. 2a and Table 1) is dominated by poorly to moderately sorted, sub-angular to rounded, horizontally bedded gravels (Gh) and granules (GRh), where gravels and granules occupy 50–100%, sand 0–50% and mud 0–40%, with common sandy to silty lenses (Sm-Fm). The average and maximum clast size is 0.1–1 cm and 5 cm, respectively. The soil thickness varies from 10–15 cm in the proximal (PD-01) and mid-fan zone (PD-02, PD-03) to 20 cm in the distal zone (PD-06). No buried palaeosoils have been detected within the profiles (Fig. 4). The lithological analysis of clasts from the PD-02 profile revealed a composition that matches the one of ME-01, suggesting local provenance from moraines and/or the wider area of the topmost parts of the Snežnik Mountain.

In addition to the geomorphological observations, the macroscopic sedimentological characterisation confirmed that the analysed PD-sediment sections were deposited in an alluvial environment. Proximal parts of alluvial fans are coarser grained and have thicker layers than distal parts, which is related to the rate of decline in gradient and consequential drop of transport energy, as typically observed in such depositional

387 environment. Inverse grading and matrix-supported fabric have not been detected

388 within the outcrops, thus we can exclude debris-flow origin. Based on resemblance

389 (i.e. clasts lithological composition, shape and size) between glacial sediments

390 described in moraines and alluvial sediments laying on the slopes bellow the

391 moraines, we interpret that the glacial sediments were the origin for alluvial

392 sediments. Transport distance of alluvial deposits was thus relatively short, between

393 several hundred meters to maximum 1.5 km. Clast roundness does not change

394 significantly from moraines to alluvial sediments, which supports the hypothesis that

395 the transport was short. Geometrical relationships between individual alluvial fans,

396 which are visible at the surface (Fig. 2a), suggest there were multiple pulses of

397 alluvial fan formation. However, based on sedimentological sections alone, the

398 individual events could not be distinguished. The alluvial fan formation process was

399 nevertheless continuous without longer periods of inactivity that would allow soil

400 formation, as suggested by the absence of buried paleosoils within investigated

401 sections. Similar thicknesses of soil cover in all investigated sections imply the

402 alluvial fans seem to be deposited at roughly the same time.

403 *4.2. ^{36}Cl exposure age*

404 Specific details of the cosmogenic samples in profile PD-02 are summarized in

405 Tables 2 (resulting chlorine concentrations), S1 (chemical sample composition) and

406 S2 (details of the sample preparation and measurement). All four samples have a

407 similar chemical composition with 51.3–54.6% of CaO (Table S1) and moderately

408 high stable chlorine concentrations (47.3–49.6 µg g^{-1}, Table 2). This indicates that

409 spallation is the main production of ^{36}Cl and that thermal neutron production has a

410 significant contribution to the total production (5-25% depending on the depth of the

411 sample, Table S2). The measured ^{36}Cl concentrations decrease with depth from

412 $5.11 \pm 0.23 \; 10^5$ atoms g^{-1} to $2.61 \pm 0.12 \; 10^5$ atoms g^{-1} for the upper three samples

413 and the ^{36}Cl concentration of the lowermost sample CRN PD-02/215-220 cm is with

414 $2.95 \pm 0.12 \; 10^5$ atoms g^{-1} slightly higher than the sample at 105–110 cm depth. The

415 ^{36}Cl and natural Cl concentration measurements of the standard material CoCal-N

416 are in a good agreement with the values obtained from other laboratories

417 (Mechernich et al., 2019).

	Denudation rate (mm ka^{-1})	Inheritance ^{36}Cl (10^5 atoms g^{-1})	Modelled ^{36}Cl conc at surface (10^5 atoms g^{-1})	Modelled age of deposition (ka)
Soil density 2.1 g cm^{-3}				
Scenario 1	0	0.61 ± 0.29	5.8 ± 0.7	11.0 ± 1.3
Scenario 2	10	0.62 ± 0.29	6.0 ± 0.7	11.6 ± 1.4
Scenario 3	**20**	**0.63 ± 0.32**	**6.2 ± 0.6**	**12.3 ± 1.7**
Scenario 4	30	0.66 ± 0.38	6.3 ± 0.5	13.3 ± 2.0
Scenario 5	40	0.59 ± 0.40	6.4 ± 0.4	14.8 ± 2.8
Scenario 6	50	0.53 ± 0.45	6.5 ± 0.4	17.0 ± 4.0
Scenario 7	60	0.46 ± 0.46	6.5 ± 0.4	20.4 ± 6.7
Soil density 1.9 g cm^{-3}				
Scenario 8	0	0.32 ± 0.31	5.6 ± 0.7	11.2 ± 1.2
Scenario 9	20	0.38 ± 0.27	6.0 ± 0.5	12.4 ± 1.4
Soil density 2.3 g cm^{-3}				
Scenario 10	0	0.63 ± 0.57	5.8 ± 0.6	10.5 ± 1.4
Scenario 11	20	0.63 ± 0.57	6.3 ± 0.5	12.0 ± 1.7

418 Table 4. ^{36}Cl modelling estimates for different scenarios of soil density and

419 denudation rates. Topographic shielding is 0.9852. No snow and vegetation shielding

420 was applied. The modelled depth profiles of scenario 1 and 3 (bold) are shown in Fig.

421 5.

422 The sediment density was estimated to 2.1 g cm^{-3} according to typical values of dry

423 unit weight of poorly graded gravel, sandy gravel, with little or no fines

424 (Geotechdata.info). Similar estimations for the density of alluvial deposits have also

425 been determined elsewhere (e.g., Machette et al., 2008; Moulin et al., 2016). The

426 influence of different denudation rates on the age calculations of alluvial deposit was

427 tested by using rates between 0 mm ka^{-1} and 60 mm ka^{-1} in steps of 10 mm ka^{-1}

428 (Table 4). These cover a range of the northern Mediterranean limestone lowering

429 rates (e.g., Cucchi et al., 1995; Plan, 2005; Furlani et al., 2009; Levenson et al.,

430 2017; Thomas et al., 2018).

431 The most likely exposure age of the alluvial deposit was computed based on an

432 iterative adaption of the pre-depositional (inherited) ^{36}Cl concentration and exposure

433 age. This adaption aimed that all four data points lie on the theoretical depth profile

434 when accounting for the 1σ uncertainties of both the data points and the ^{36}Cl

435 production rates (Fig. 5). All depth profiles indicate that the ^{36}Cl concentration of the

436 lowermost sample CRN PD-02/215-220 cm is too high compared to the ^{36}Cl

437 concentration of the other three samples (Fig. 5). Hence, it was excluded from the

438 curve fitting. The resulting depth profiles lead to a minimum age of the alluvial deposit

439 of 11.0 ± 1.3 ka when assuming no denudation up to an age of 13.3 ± 2.0 ka for a

440 likely rate of 30 mm ka^{-1} of denudation. For higher denudation rates the modelled

441 ages and age uncertainties get significantly higher, e.g., 20.4 ± 6.7 ka for 60 mm ka^{-1}

442 of denudation (Table 4). Age uncertainties related to the influence of different soil

443 densities are negligible compared to the uncertainties related to the ^{36}Cl
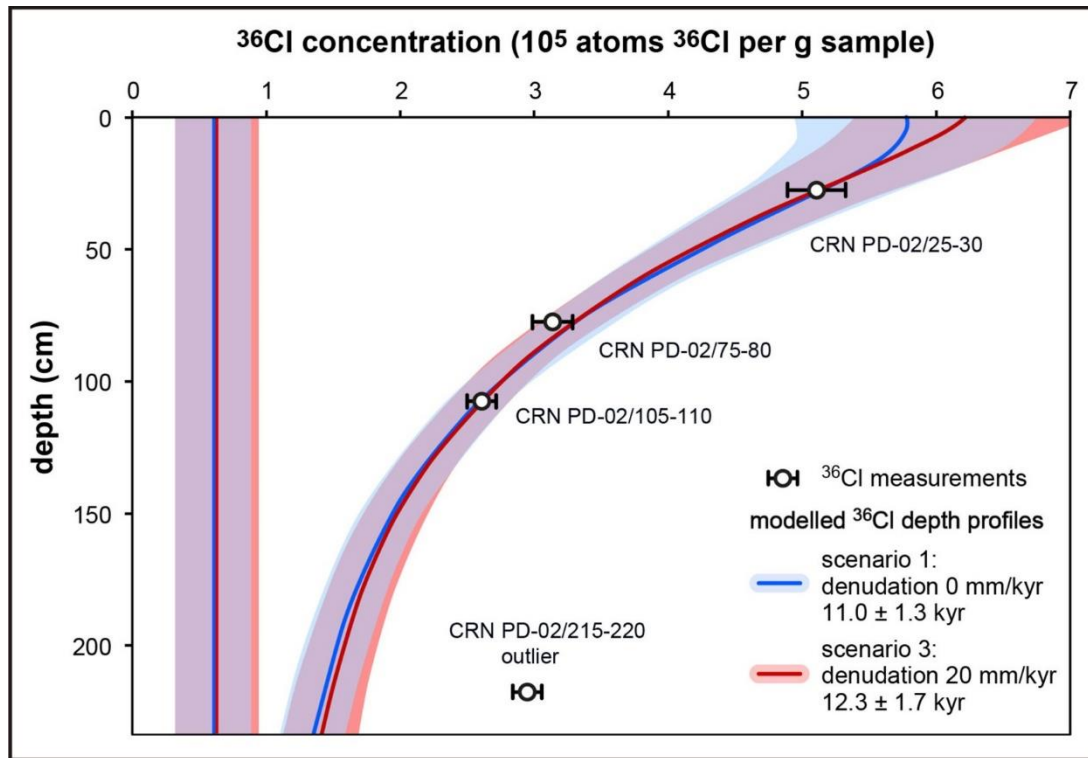
444 concentration measurements or the denudation rates.

Fig. 5. [36]Cl concentration as a function of depth on the alluvial fan at site PD-02. Data points (circles) are derived from the amalgamated limestone pebble samples (Table 2). The (1σ) analytical uncertainties in [36]Cl concentration were incorporated in the model optimization. The modelled [36]Cl depth profiles of the [36]Cl concentration of the tested scenarios are similar (Table 4) and for better overview, we show only the exposure model optimization using denudation rates of 0 (blue) and 20 mm ka[-1] (red) and a soil density of 2.1 g cm^{-3}. The vertical line with its uncertainty represents the hypothetical pre-depositional [36]Cl component and the exponential curved represents the modelled total concentration.

4.3.   Inverse ERT models

The resistivity distribution of the inverse ERT models shows well-contrasted resistivity bodies that are being described in terms of geological layers based on the geomorphological and sedimentological characterization of the study area and representative resistivity ranges for similar rocks/sediments (Table 3).
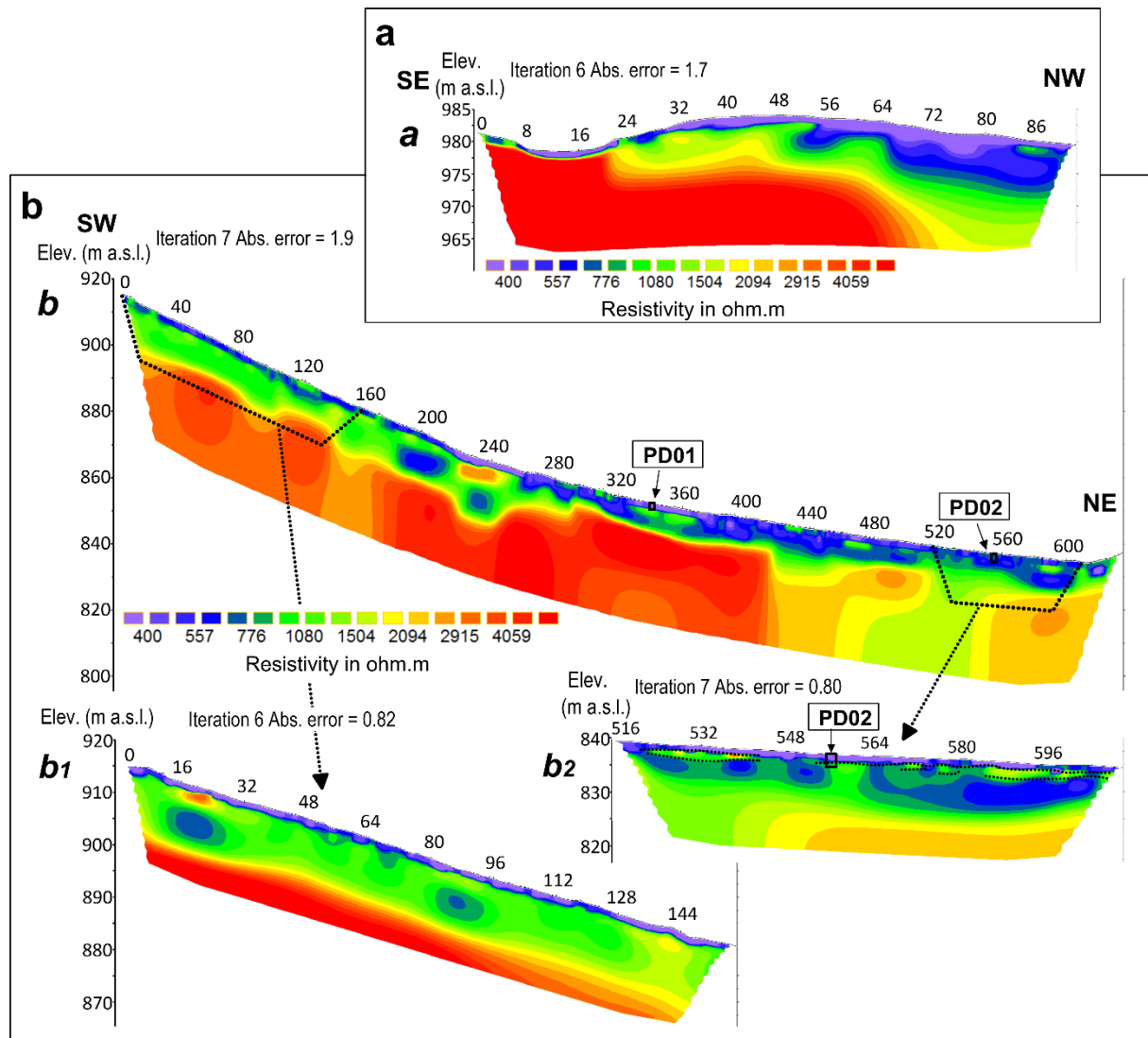
Fig. 6. Inverse ERT models of (a) Profile a and (b) Profile b with higher resolution sections b_1 and b_2 (occasionally washed out horizon is marked with black dotted line). Distance is shown in meters on the top of each profile.

4.3.1. Profile a (Figs. 2a and 6a)

The low resistivity area (200–900 Ωm) with thickness up to ~8 m at the top of the profile, corresponds to the glacial deposits described in the outcrop ME-03 (Figs. 2 and 3), located ~50 m to the SW of Profile a. The medium (900–1500 Ωm) resistivity body with thickness up to ~6 m (and depth up to ~14 m) located below, might either correspond to the same, but coarser and/or less saturated glacial deposits, or even to the stratigraphically older glacial deposits. In the latter case, the relatively higher

471 resistivity values could be due to a higher degree of cementation, resulting in lower

472 porosity and lower moisture content. The highest resistivity body (3000–6000 Ωm) in

473 the lower part of the ERT image corresponds to the solid limestone bedrock, which

474 crops out on the SE side of the profile and is buried below glacial deposits towards

475 NW. The relatively high resistivity corrugated area (1500–2000 Ωm) overlying the

476 limestone bedrock reflects glacially reshaped bedrock with fissured and weathered

477 limestone.

478 *4.3.2. Profile b (Fig. 2a and 6b)*

479 The highest resistivity area (2500–6000 Ωm) corresponds to the limestone bedrock,

480 wherein subvertical fault is likely present at ~160 m of the profile distance (at the

481 area of 2500 Ωm). Bedrock lies between ~7 m and 20 m below the surface, having

482 an undulated shape in the first 280 m of the profile length. The low resistivity

483 (sub)vertical zone within the bedrock (1500–2500 Ωm) starts at 420 m of the profile

484 length and continues to the end of the profile, indicating a fault zone is present in the

485 limestone bedrock.

486 The top layer with lower resistivity (200–900 Ωm, locally 1000 Ωm) along the whole

487 Profile b belongs to deposits consisting of coarse-gravel facies (PD-01 and PD-02 in

488 Fig. 4).The thickness (and depth) of these sediments amounts to ~2 m in the first 260

489 m of the profile distance, and 5–10 m at lower altitudes. The higher resistivity

490 interrupted layer of up to ~1000–2000 Ωm that can be observed at higher resolution

491 section b_2 (marked with black dotted line in Fig. 6b-b_1) within a relatively homogenous

492 resistivity body can be explained in terms of coarser sediment and/or washed out

493 horizon, described at the bottom of the PD-02 profile. It might also indicate the

494 boundary between younger and older alluvial deposits.

495   Two relatively homogenous medium resistivity areas (900–1500 Ωm) are present

496   between bedrock and near-surface low resistivity alluvial deposits. The first is

497   positioned on the SW slope and the second lies on the NE side of the Profile b above

498   the bedrock fault zone. The first medium resistivity body (900–1500 Ωm) above the

499   bedrock is relatively homogenous in the first 180 m of the profile distance, with

500   average thickness of ~10–12 m. This continues along the profile to a less

501   homogenous section at 180–280 m of the profile distance with two lower resistivity

502   areas (~600 Ωm) and one higher resistivity block (~2500 Ωm). However, a bigger

503   portion of the area still reaches resistivity values of 900–1500 Ωm, thus it can be

504   considered as a relatively uniform sediment body with local resistivity abruptions. A

505   sharp resistivity transition (2.5 to 5 fold) to the underlying limestone bedrock clearly

506   separates the whole sequence from the bedrock. According to the vicinity of

507   outcropping glacial deposits (Fig. 2a), the described sediment body likely represents

508   coarser (and less saturated) or even cemented glacial deposits, resulting in higher

509   resistivity values with respect to the glacial deposits present at the surface of the

510   Profile a. The whole section might correspond to alluvial deposits if we consider that

511   the bottom resistivity of PD-01 and PD-02 trenches reaches up to 1000 Ωm and the

512   fact that the proximal part of alluvial fans are coarser grained and have thicker layers

513   than distal parts. However, this interpretation is less likely.

514   The second area having similar resistivity values (900–1500 Ωm) is largely situated

515   above the fault zone with thickness up to ~8 m (and reaching depth up to ~15 m).

516   Based on resistivity values and its superposition it likely represents stratigraphically

517   older alluvial deposits.

5. Discussion

5.1.   Subsurface stratigraphy

Based on ERT results, we propose two interpretations in terms of different

stratigraphy of the medium resistivity bodies, while bedrock (B), fault zone (B-FZ) and

fractured bedrock (B-FW) remain the same in both interpretations. The first

interpretation (Fig. 7a) is consistent with the geomorphological and sedimentological

data observed on the field, while the second interpretation (Fig. 7b) is furthermore

consistent in terms of similarities in resistivity ranges. However, the GD0 sediment

body in the second interpretation cannot be associated with any of the mapped

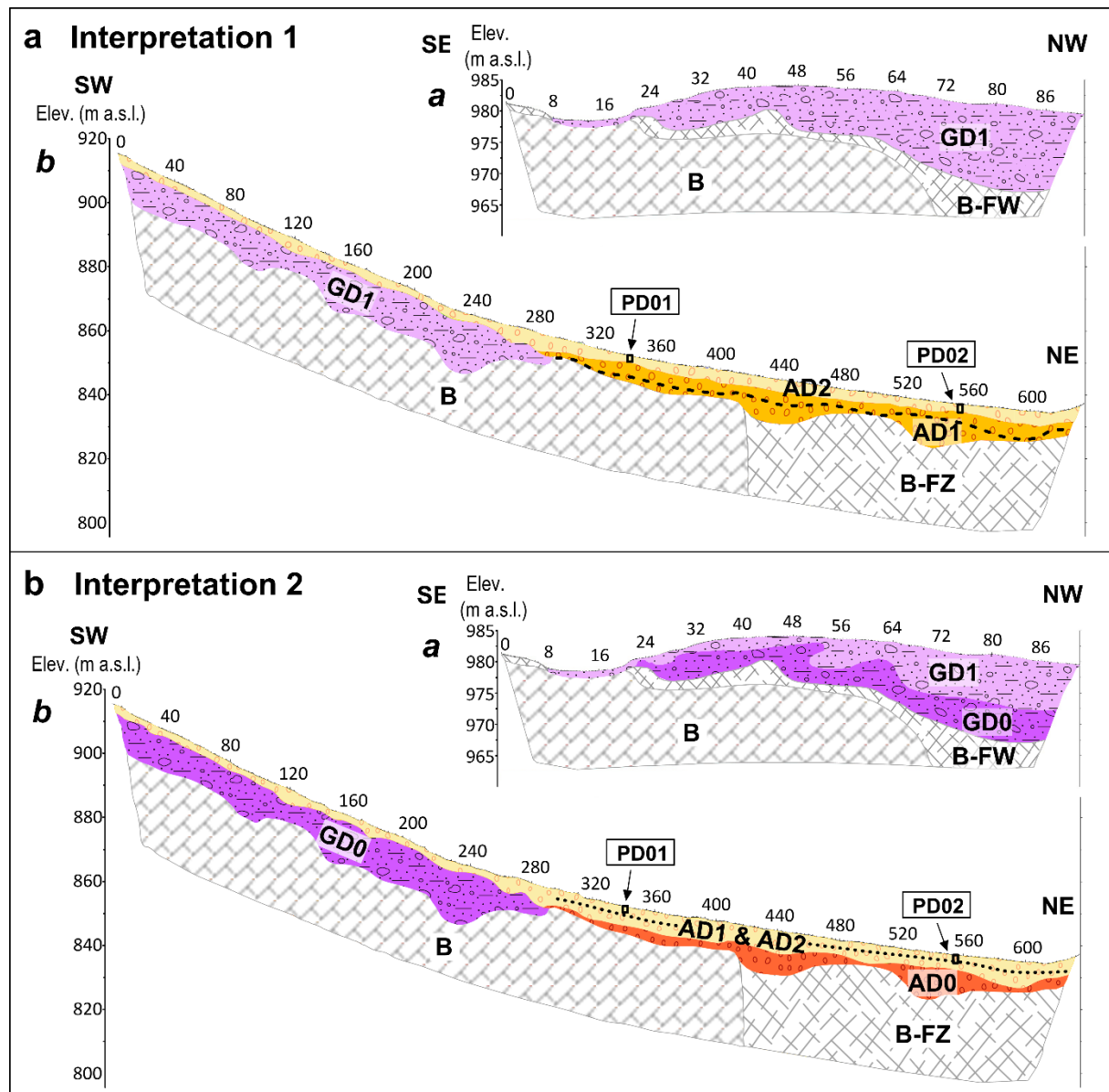geomorphological features on the surface.

Fig. 7. The two most probable interpretations of the ERT models: a) Interpretation 1, and b) Interpretation 2. Distance (in meters) is shown on the top of each profile. B – limestone bedrock, B-FZ – fault zone in limestone bedrock, B-FW – fractured and/or weathered bedrock, GD0 – oldest glacial deposits related to pre – LGM glaciation, GD1 – older glacial deposits related to LGM, AD0 – alluvial deposits related to GD0, AD1 – alluvial deposits related to GD1, AD2 – youngest alluvial deposits (dated to Younger Dryas).

5.1.1. Interpretation 1

537 In Profile a, the whole resistivity range of 200–1500 Ωm, with thickness up to ~14 m,

538 is interpreted as the glacial deposit GD1 observed in the ME-03 outcrop. The same

539 interpretation was made for the ~10–12 m thick buried sediment body in the first 280

540 m of the Profile b (900–1500 Ωm), which is a continuation of the right lateral moraine,

541 located 10 m higher and 70 m further towards SW. Slightly higher resistivity values of

542 GD1 in Profile b with respect to GD1 in Profile a can be related to a decreasing

543 amount of matrix towards palaeo-ice margin, where till deposits gradually pass over

544 to alluvial deposits, which is also supported by our observations from several

545 outcrops (Figs. 3 and 4). Variable resistivity values within both GD1 sediment bodies

546 are likely a result of local differences in saturation and clast size.

547 The whole surface of the Profile b is covered by the youngest alluvial deposits AD2

548 (200–900 Ωm, locally 1000 Ωm), observed in the PD-01 and PD-02 trenches. These

549 overlay glacial deposits GD1 in the first 280 m of the profile and stratigraphically

550 older alluvial deposits AD1 in the rest of the profile. While the boundary between

551 GD1 and AD2 is well justified with the differences in resistivity, it is more difficult to

552 depict the boundary between AD1 and AD2. One possibility is to place the boundary

553 at the highest contrast in resistivity values between the lower (900–1500 Ωm) and

554 upper (200–900 Ωm, with thin interrupted layer ~1000–2000 Ωm) alluvial deposits

555 (marked with black dashed line on Profile b in Fig. 7a). This would suggest that a

556 difference in resistivity is due to the size of clasts, that is coarser in AD1 with respect

557 to AD2, which can be explained by the distance from the palaeo-ice margin. Having

558 the palaeo-ice margin marked with glacial deposits GD1, then AD1 can be

559 considered as proximal, coarser alluvial deposits and AD2 as distal, finer alluvial

560 deposits. According to this interpretation AD2 is concurrent with glacial deposits GD2

561 (Fig. 2a), and thus the difference in resistivity between AD1 and AD2 might as well

562 be associated with a different degree of cementation and/or presence of washed-out

563 horizons, which have been recognised in the PD-02 log (Fig. 4) within AD2 unit

564 (section b_2 in Fig. 6b). Both conditions would result in higher resistivity values, since

565 they would lead to reduced moisture content in sediments, common for high altitude

566 karst environment, where vertical drainage and consequently no broader long-term

567 saturation zones are present. In this hypothesis the thickness (and depth) of AD1 is

568 up to 10 m, while the thickness and depth of AD2 is up to 8 m and 15 m, respectively.

569 An alternative boundary between AD1 and AD2 (marked with lighter and darker

570 yellow colour on Profile b in Fig. 7a) can be depicted at the depth of the lowermost

571 sample in PD-02, recognized as an age outlier. This sample most probably belongs

572 to an older depositional event and hence experienced longer exposure history,

573 resulting in the relatively high ^{36}Cl concentration, which does not fit into the depth

574 profile curve (Fig. 5). This cannot be directly supported with the results of the

575 sedimentological analyses since no erosional discontinuities were detected within the

576 outcrop. However, washed-out and occasionally cemented horizons at a depth of

577 155–180 cm in PD-02 (Fig. 4) indicate a likely short interruption in deposition and

578 thus a boundary between two events. This interpretation is supported by obvious

579 vertical changes of resistivity values in alluvial deposits on the higher-resolution ERT

580 section b_2, where thin higher resistivity layer (~1000–2000 Ωm) is present at a depth

581 interval of ~1.5–3 m (marked with black dotted line in section b_2 of Fig. 6b), within the

582 layer otherwise characterized by resistivity values of 200–900 Ωm. In this case, the

583 higher resistivity values indicate occasionally washed-out horizons within alluvial

584 deposits. The thin higher resistivity layer is also laterally discontinuous, suggesting

585 the channel-network formation. The thickness (and depth) of AD2 according to this

586 interpretation is up to 3 m, and the thickness and depth of AD1 is up to 12 m and 15

587 m, respectively.

5.1.2. Interpretation 2

589 Interpretation 2 associates higher resistivity values (900–1500 Ωm) of the GD1 and

590 AD1 sediment bodies in the interpretation 1 with higher degree of sediment

591 cementation. These sections are marked with GD0 and AD0 in Fig. 7b and are in a

592 stratigraphically older position from GD1 and AD1. This implies GD0, not visible on

593 the surface, points to a larger glacier extent from GD1, which is now present only as

594 top layer in Profile a with resistivity values of 200–900 Ωm and thickness up to ~8 m.

595 In this interpretation, the alluvial deposits AD0 have the same resistivity range as

596 glacial deposits GD0 (900–1500 Ωm) and reach thickness and depth up to ~8 m and

597 ~15 m, respectively. GD0 in Profile a show severely undulated surface, suggesting

598 they were subglacially deformed. The thickness of GD0 reaches up to ~6 m in Profile

599 a and ~10–12 m in Profile b.

600 Again, the border between AD1 and AD2 (marked with black dotted line on Profile b

601 in Fig. 7b) is not entirely clear. This border is associated with the depth of the age

602 outlier and washed-out horizons in the PD-02, supported by anomalous higher

603 resistivity layer on section b_2. Thus, AD1 has resistivity values in the range of 500–

604 900 Ωm, with an exception of laterally discontinuous washed out horizons, having

605 values of ~1000–2000 Ωm. In this interpretation, the thickness of AD0 is up to 8 m,

606 for AD1 up to 4 m and for AD2 up to 3 m.

5.2. Uncertainties and assumptions of the cosmogenic [36]Cl exposure age

608 Cosmogenic [36]Cl nuclide dating modelling estimate suggests an age of 12.3 ± 1.7 ka

609 (1σ) as the most probable age of the dated alluvial deposits (PD-02 within the AD2

610   unit) in the Praprotna draga depression by using 2.1 g cm^{-3} for a density of deposits

611   and 20 mm ka^{-1} for a denudation rate. Both parameters were estimated and

612   considered as most probable using previously published data and taking into account

613   the local characteristics. Although the density of coarse-grained deposits is difficult to

614   determine accurately, a variation of ± 0.2 g cm^{-3} change the exposure age only by ±

615   0.3 ka.

616   The study area is characterized by high MAP (>2500 mm) and the dominant lithology

617   of the dated clasts is Cretaceous limestone. These lithological and climate

618   characteristics are roughly similar to those in the Classical Karst area, where the

619   mean limestone bedrock lowering rate of 18 mm ka^{-1} was measured within a period

620   of up to 26 years using micro-erosion meter (Furlani et al., 2009). Even higher

621   denudation rates (30–60 mm ka^{-1}) were measured on the exposed carbonate

622   bedrock in SE France (Thomas et al., 2018) and elsewhere in the Mediterranean

623   (Levenson et al., 2017 and references therein). Denudation rates determined on

624   Mediterranean and central European sediments also vary distinctly and appear to be

625   within similar range (10–80 mm ka^{-1}; e.g., Siame et al., 2004; Ryb et al., 2014;

626   Ruszkiczay-Rüdiger et al., 2016a). Nevertheless, our study area receives more

627   precipitation than the nearby Classical Karst (MAP: 1340 mm; Furlani et al., 2009)

628   and the material is not bedrock but alluvial material, which both suggest that the

629   denudation rate is likely to be higher.

630   The age modelling does not consider a correction for snow shielding, although the

631   continental climate and the high precipitation imply a substantial snow cover in the

632   study area. This is related to the difficult quantification of the effect of the snow cover,

633   since on one hand the snow cover reduces the production of the target elements, but

634   on the other hand the hydrogen rich cover increases the production rate based on

635 thermal neutrons. This rate can get significant in the case of the moderate

636 concentrations of stable Cl in the samples (Dunai et al., 2014; Gromig et al., 2018).

637 It is clear from Table 4 that applying a range of relevant denudation rates for

638 correcting exposure ages will have a great impact on the correct age of the landform.

639 For example, if different estimates of soil density and denudation are used, the

640 resulting age falls within a range of ~ 9–21 ka (1σ uncertainties), which will shift our

641 most likely age interpretation from Younger Dryas to Holocene, Oldest Dryas or even

642 LGM. The impact of other published ^{36}Cl production rates (e.g., Marrero et al.,

643 2016b), or the inclusion of estimates of snow or vegetation interactions is negligible

644 within the 1σ age range.

645 *5.3.   Time frame from glacial to non-glacial conditions*

646 Based on the distribution of glacial deposits on the surface in the Praprotna draga

647 hinterland and their morphological expression (Fig. 2a), at least two glacial phases

648 with an altitudinal difference in glacier fronts of ~140 m can be distinguished.

649 Glaciers in the older phase (Glacial stage 1 in Fig. 2b) almost reached the bottom of

650 the depression at 860–910 m a.s.l., while in the younger phase (Glacial stage 2 in

651 Fig. 2b) they retreated back to ~1050 m a.s.l. The two-phase interpretation is also

652 supported by the Interpretation 1 of the ERT models (Fig. 7a) performed along the

653 northernmost alluvial fan, which show a diamicton-like sedimentary body (GD1)

654 buried below alluvial deposits (AD2). This is the most probable interpretation of the

655 ERT models, because it is well supported with the observed geomorphological and

656 sedimentological data in the study area. An alternative explanation, based only on

657 the Interpretation 2 of the ERT models (Fig. 7b) suggests that GD1 in Interpretation 1

658 are in fact older GD0 glacial deposits that do not correlate with any of the mapped

659 moraines on the surface. They might belong to an older and slightly larger glaciation

660   from Glacial stage 1. Although the exact timeframe of glacial phases is still unknown,

661   we can make some assumptions about their age by taking into account the

662   equilibrium line altitudes (ELAs) estimated for the neighbouring past glacierized

663   areas and based on the correlation with the results from the nearby Gomance area

664   (Fig. 1).

665   The equilibrium line altitude (ELA) for the Glacial stage 1 glaciers was calculated by

666   Žebre (2015) to 1325-1282 m using a range of representative modern area altitude

667   balance ratios (AABR) of 1.5-3.5 (Osmaston, 2005; Rea, 2009) and 1324 m by

668   applying the accumulation-area ratio (AAR) of 0.6. Similarly low ELAs were estimated

669   for the largest, tentatively Last glaciation for the nearby Julian Prealps (ELA ~1130-

670   1200 m) (Monegato, 2012) and for the Trnovski gozd plateau (ELA ~1255-1216 m)

671   (Žebre et al., 2013) using the AABR method. Low ELA values (ELA ~1256 m) in the

672   Balkans were calculated using the AAR of 0.8 only for the glaciers dated to MIS 12 in

673   the coastal Orjen Mountain (Montenegro) receiving high modern MAP (~5000 mm),

674   while during the Last glaciation the ELA was calculated to 1456 m using AAR of 0.5

675   (Hughes et al., 2010). The minimum ELAs estimated for other mountains in the

676   Balkans that are located more inland, were substantially higher (ELA ~1600-2200 m)

677   (e.g., Kuhlemann et al., 2009, 2013; Hughes et al., 2011; Ribolini et al., 2011). This

678   suggests that a correlation with the Snežnik Mountain is less reasonable. Based on

679   ELA correlations and the stratigraphic relationship with the deposits filling the

680   Gomance karst depressions (see Introduction and references therein), the Glacial

681   stage 1 can be potentially linked to the Last glaciation, although an older age is not to

682   be excluded, as suggested by other studies in the Balkan Peninsula (e.g., Hughes et

683   al., 2006, 2010, 2011). The latter is a more likely explanation for the GD0 glacial

684   deposits if considering the Interpretation 2 of subsurface stratigraphy as being

correct. However, estimating the ELA for the younger, Glacial stage 2, is subject to more uncertainties, because at that time Snežnik was still covered with an ice field, hence its extent is difficult to determine owing to karst topography and missing geomorphological evidence in some places. Assuming the Glacial stage 1 belongs to the LGM, then the Glacial stage 2 can be associated with the first recessional phase after the LGM (e.g., Oldest Dryas; ca. 17.5–14.5 ka). It is unlikely that the Glacial stage 2 would belong to the Younger Dryas (YD) phase (12.9–11.7 ka). Based on the findings from other studies in the Balkans, (e.g., Kuhlemann et al., 2009; Hughes et al., 2010; Ribolini et al., 2011; Pope et al., 2015), the YD ELA was on average 180 m higher with respect to the LGM ELA. In the Alps, the YD-LGM differences in ELA were even greater (> 650 m) (Ivy-Ochs, 2015). Applying the average-recorded YD-LGM ELA difference to Snežnik results in the YD ELA of ~1500 m. An ELA at this high altitude suggests that the accumulation area would be too small for glaciers to reach down to 1050 m a.s.l., where the Glacial stage 2 moraines are deposited. The YD glaciation in the form of small cirque glaciers was established on five mountain massifs in the Balkans (see Introduction section) but cannot be confirmed on Snežnik, which is in agreement with the findings from the Pelister Mountain (Macedonia) (Ribolini et al., 2018). Here we propose that the dated and also the youngest alluvial deposits (i.e. the uppermost ~2 m within AD2 stratigraphic unit) in Praprotna draga were not deposited directly by meltwaters, although the cosmogenic dating of the PD-02 depth profile suggests they were deposited during the YD cooling at 12.3 ± 1.7 ka. Hence, we can assume that the youngest deposition took place some thousands of years after the glacier retreat during the transition period from glacial to non-glacial conditions, when the slope denudation and remobilization of pre-existing glacigenic sediments reinitiated fan aggradation. Our findings suggest

710 that the time window of paraglacial adjustment in Snežnik was brief and that it ended

711 in YD, which is unlike in the adjacent SE Alps, which are still recovering from the Last

712 glaciation and undergoing paraglacial sediment reworking also in the present climate

713 (Bavec et al., 2004; Bavec and Verbič, 2011). A short-lived paraglacial period,

714 explained by a quick expansion of dense forest and subsequent stabilization of

715 deglaciating terrain has been suggested also for other Mediterranean mountains

716 (Woodward et al., 2014; Delmas et al., 2015).

717 We therefore argue that a brief paraglacial response to the last deglaciation was not

718 only conditioned by the quick expansion of dense forest (Woodward et al., 2014), but

719 also by the inefficient surface runoff on deglaciated karst terrain. During glacial

720 advances, surface runoff prevailed towards glacier margins and karst depressions

721 received large sediment fluxes from meltwaters. In the course of deglaciation, a

722 subterranean drainage started to prevail due to exposed limestone bedrock areas

723 and reduced sediment load, favouring the quick adjustment of relief to non-glacial

724 conditions and preservation of sediment fill. At present, the dominant pathway for

725 runoff is the karst network and the chemical weathering of the surface is the main

726 process in the study area, while slope processes are mainly limited to steep slopes

727 and/or mechanically less resistant lithology. This results in almost negligible sediment

728 supply, leaving the fans inactive at present and their surfaces well vegetated.

729 **6. Conclusions**

730 We studied a well-preserved sediment infill of the Praprotna draga karst depression

731 in the deglaciated Snežnik Mountain (Slovenia) by applying various methods, such

732 as geomorphological mapping, sediment facies analysis, ERT measurements and

733 cosmogenic ^{36}Cl nuclide exposure dating. According to the Interpretation 1 of ERT

models, which is well supported by geomorphological and sedimentological data, we divided subsurface stratigraphy in glacial (GD1) and alluvial deposits (AD1), associated with the LGM and buried by alluvial deposits (AD2), linked to Late-glacial. The topmost ~2 m of AD2 was dated to the Younger Dryas cooling at 12.3 ± 1.7 ka. The existence of the Younger Dryas glaciers in Snežnik is unlikely based on the equilibrium line altitude reconstructions, hence we propose that the youngest alluvial deposits of the Late-glacial aggradation phase (AD2) relate with the paraglacial period that ended in Younger Dryas. Our findings suggest that the time window of paraglacial adjustment in Snežnik was short, and it depended largely on the karst geomorphic system and quick vegetation change. We also demonstrate that the sediment supply in karst areas during glacial and paraglacial periods contrast sharply with present-day conditions, owing mainly to a change in the type of drainage (surface versus underground). Our results are subject to uncertainty because of some assumptions regarding the exact time of glacier retreat. Therefore, further work on the age of glacier stabilization and improvement of the alluvial fan chronology is needed.

References

Adamson, K.R., Woodward, J.C., Hughes, P.D., 2014. Glaciers and rivers: Pleistocene uncoupling in a Mediterranean mountain karst. Quat. Sci. Rev. 94, 28–43. https://doi.org/10.1016/j.quascirev.2014.04.016

Athanasiou, E.N., Tsourlos, P.I., Papazachos, C.B., Tsokas, G.N., 2007. Combined weighted inversion of electrical resistivity data arising from different array types. J. Appl. Geophys. 62, 124–140. https://doi.org/10.1016/j.jappgeo.2006.09.003

Ballantyne, C.K., 2002. Paraglacial geomorphology. Quat. Sci. Rev. 21, 1935–2017. https://doi.org/https://doi.org/10.1016/S0277-3791(02)00005-7

Ballantyne, C.K., 2003. Paraglacial landform succession and sediment storage in deglaciated mountain valleys: theory and approaches to calibration. Zeitschrift für Geomorphol. Suppl. 132, 1–18.

Bavec, M., Verbič, T., 2011. Glacial history of Slovenia, in: Horne, D.J., Holmes, J.A., Rodriguez-Lazaro, J., Viehberg, F.A. (Eds.), Developments in Quaternary Science. pp. 385–392. https://doi.org/10.1016/B978-0-444-53447-7.00029-5

Bavec, M., Tulaczyk, S.M., Mahan, S.A., Stock, G.M., 2004. Late Quaternary glaciation of the Upper Soča River Region (Southern Julian Alps, NW Slovenia). Sediment. Geol. 165, 265–283. https://doi.org/10.1016/j.sedgeo.2003.11.011

Braucher, R., Merchel, S., Borgomano, J., Bourlès, D.L., 2011. Production of cosmogenic radionuclides at great depth: A multi element approach. Earth Planet. Sci. Lett. 309, 1–9. https://doi.org/10.1016/j.epsl.2011.06.036

Ćalić, J., 2011. Karstic uvala revisited: Toward a redefinition of the term.

780   Geomorphology 134, 32–42. https://doi.org/10.1016/J.GEOMORPH.2011.06.029

781 Church, M., Slaymaker, O., 1989. Disequilibrium of Holocene sediment yield in

782   glaciated British Columbia. Nature 337, 452. https://doi.org/10.1038/337452a0

783 Claerbout, J.F., Muir, F., 1973. Robust modeling with erratic data. Geophysics 38,

784   826–844.

785 Colucci, R.R., 2016. Geomorphic influence on small glacier response to post-Little

786   Ice Age climate warming: Julian Alps, Europe. Earth Surf. Process. Landforms

787   41, 1227–1240. https://doi.org/10.1002/esp.3908

788 Colucci, R.R., Boccali, C., Žebre, M., Guglielmin, M., 2016. Rock glaciers, protalus

789   ramparts and pronival ramparts in the south-eastern Alps. Geomorphology 269,

790   112–121. https://doi.org/10.1016/j.geomorph.2016.06.039

791 Cordier, S., Adamson, K., Delmas, M., Calvet, M., Harmand, D., 2017. Of ice and

792   water: Quaternary fluvial response to glacial forcing. Quat. Sci. Rev. 166, 57–73.

793   https://doi.org/10.1016/J.QUASCIREV.2017.02.006

794 Cucchi, F., Forti, F., Marinetti, E., 1995. Surface degradation of carbonate rocks in

795   the Karst of Trieste (Classical Karst, Italy), in: Formos, J.J., Ginés, A. (Eds.),

796   Karren Landforms. Palma, pp. 41–51.

797 Cvijić, J., 1893. Das Karstphänomen. Geogr. Abhandlungen 5, 218–329.

798 Delmas, M., Braucher, R., Gunnell, Y., Guillou, V., Calvet, M., Bourlès, D., 2015.

799   Constraints on Pleistocene glaciofluvial terrace age and related soil

800   chronosequence features from vertical 10Be profiles in the Ariège River

801   catchment (Pyrenees, France). Glob. Planet. Change 132, 39–53.

802   https://doi.org/10.1016/J.GLOPLACHA.2015.06.011

803   Dunai, T., 2010. Cosmogenic Nuclides Principles, Concepts and Applications in the

804   Earth Surface Sciences. Cambridge Academic Press, pp 198.

805   Dunai, T.J., Binnie, S.A., Hein, A.S., Paling, S.M., 2014. The effects of a hydrogen-

806   rich ground cover on cosmogenic thermal neutrons: Implications for exposure

807   dating. Quat. Geochronol. 22, 183–191.

808   https://doi.org/10.1016/j.quageo.2013.01.001

809   Evans, D.J.A., Benn, D.I. (Eds.), 2004. A practical guide to the study of glacial

810   sediments. Arnold, London. pp. 280.

811   Fink, D., Vogt, S., Hotchkis, M., 2000. Cross-sections for 36Cl from Ti at Ep=35–150

812   MeV: Applications to in-situ exposure dating. Nucl. Instruments Methods Phys.

813   Res. Sect. B Beam Interact. with Mater. Atoms 172, 861–866.

814   https://doi.org/10.1016/S0168-583X(00)00200-7

815   Frankel, K.L., Brantley, K.S., Dolan, J.F., Finkel, R.C., Klinger, R.E., Knott, J.R.,

816   Machette, M.N., Owen, L.A., Phillips, F.M., Slate, J.L., Wernicke, B.P., 2007.

817   Cosmogenic 10Be and 36Cl geochronology of offset alluvial fans along the

818   northern Death Valley fault zone: Implications for transient strain in the eastern

819   California shear zone. J. Geophys. Res. Solid Earth 112, B06407.

820   https://doi.org/10.1029/2006JB004350

821   Furlani, S., Cucchi, F., Forti, F., Rossi, A., 2009. Comparison between coastal and

822   inland Karst limestone lowering rates in the northeastern Adriatic Region (Italy

823   and Croatia). Geomorphology 104, 73–81.

824   https://doi.org/10.1016/J.GEOMORPH.2008.05.015

825   Grlj, A., Grigillo, D., 2014. Uporaba digitalnega modela višin in satelitskega posnetka

826   RapidEye za zaznavanje kraških kotanj in brezstropih jam Podgorskega krasa =

827   Use of digital elevation model and RapidEye satellite image to locate karst

828   depressions and unroofed caves of Podgorski. Dela 42, 129–147.

829   https://doi.org/10.4312/dela.42.7.129-147

830   Gromig, R., Mechernich, S., Ribolini, A., Wagner, B., Zanchetta, G., Isola, I., Bini, M.,

831   Dunai, T.J., 2018. Evidence for a Younger Dryas deglaciation in the Galicica

832   Mountains (FYROM) from cosmogenic 36Cl. Quat. Int. 464, 352–363.

833   https://doi.org/10.1016/j.quaint.2017.07.013

834   Hancock, G.S., Anderson, R.S., Chadwick, O.A., Finkel, R.C., 1999. Dating fluvial

835   terraces with 10Be and 26Al profiles: application to the Wind River, Wyoming.

836   Geomorphology 27, 41–60. https://doi.org/https://doi.org/10.1016/S0169-

837   555X(98)00089-0

838   Harbor, J., Warburton, J., 1993. Relative Rates of Glacial and Nonglacial Erosion in

839   Alpine Environments. Arct. Alp. Res. 25, 1–7.

840   Hein, A.S., Hulton, N.R.J., Dunai, T.J., Schnabel, C., Kaplan, M.R., Naylor, M., Xu,

841   S., 2009. Middle Pleistocene glaciation in Patagonia dated by cosmogenic-

842   nuclide measurements on outwash gravels. Earth Planet. Sci. Lett. 286, 184–

843   197. https://doi.org/https://doi.org/10.1016/j.epsl.2009.06.026

844   Hughes, P.D., Woodward, J.C., Gibbard, P.L., Macklin, M.G., Gilmour, M.A., Smith,

845   G.R., 2006. The Glacial History of the Pindus Mountains, Greece. J. Geol. 114,

846   413–434. https://doi.org/10.1086/504177

847   Hughes, P.D., Woodward, J.C., van Calsteren, P.C., Thomas, L.E., 2011. The glacial

history of the Dinaric Alps, Montenegro. Quat. Sci. Rev. 30, 3393–3412.
https://doi.org/10.1016/j.quascirev.2011.08.016

Hughes, P.D., Woodward, J.C., van Calsteren, P.C., Thomas, L.E., Adamson, K.R.,
2010. Pleistocene ice caps on the coastal mountains of the Adriatic Sea. Quat.
Sci. Rev. 29, 3690–3708. https://doi.org/10.1016/j.quascirev.2010.06.032

Isotta, F.A., Frei, C., Weilguni, V., Perčec Tadić, M., Lassègues, P., Rudolf, B.,
Pavan, V., Cacciamani, C., Antolini, G., Ratto, S.M., Munari, M., Micheletti, S.,
Bonati, V., Lussana, C., Ronchi, C., Panettieri, E., Marigo, G., Vertačnik, G.,
2014. The climate of daily precipitation in the Alps: development and analysis of
a high-resolution grid dataset from pan-Alpine rain-gauge data. Int. J. Climatol.
34, 1657–1675. https://doi.org/10.1002/joc.3794

Ivy-Ochs, S., 2015. Glacier variations in the European Alps at the end of the last
glaciation. Cuad. Investig. Geográfica 41, 295–315.

Kobal, M., Bertoncelj, I., Pirotti, F., Dakskobler, I., Kutnar, L., 2015. Using Lidar Data
to Analyse Sinkhole Characteristics Relevant for Understory Vegetation under
Forest Cover—Case Study of a High Karst Area in the Dinaric Mountains. PLoS
One 10, 1–19. https://doi.org/10.1371/journal.pone.0122070

Komac, B., Hrvatin, M., Perko, D., Natek, K., Mihevc, A., Prelovšek, M., Zorn, M.,
Stepišnik, U., 2012. Recent Landform Evolution in Slovenia, in: Stankoviansky,
M., Lóczy, D., Kotarba, A. (Eds.), Recent Landform Evolution: The Carpatho-
Balkan-Dinaric Region. Springer, pp. 287–311.

Kowalczyk, S., Maślakowski, M., Tucholka, P., 2014. Determination of the correlation
between the electrical resistivity of non-cohesive soils and the degree of

871   compaction. J. Appl. Geophys. 110, 43–50.

872   https://doi.org/10.1016/j.jappgeo.2014.08.016

873   Kranjc, A., 2010. Short History of Research, in: Mihevc, A., Prelovšek, M., Zupan

874   Hajna, N. (Eds.), Introduction to the Dinaric Karst. Karst Research Institute at

875   ZRC SAZU, Postojna, pp. 9–13.

876   Krklec, K., Domínguez-Villar, D., Perica, D., 2015. Depositional environments and

877   diagenesis of a carbonate till from a Quaternary paleoglacier sequence in the

878   Southern Velebit Mountain (Croatia). Palaeogeogr. Palaeoclimatol. Palaeoecol.

879   436, 188–198. https://doi.org/10.1016/J.PALAEO.2015.07.004

880   Kuhlemann, J., Gachev, E., Gikov, A., Nedkov, S., Krumrei, I., Kubik, P., 2013.

881   Glaciation in the Rila mountains (Bulgaria) during the Last Glacial Maximum.

882   Quat. Int. 293, 51–62. https://doi.org/10.1016/J.QUAINT.2012.06.027

883   Kuhlemann, J., Milivojević, M., Krumrei, I., Kubik, P.W., 2009. Last glaciation of the

884   Šara Range (Balkan peninsula): Increasing dryness from the LGM to the

885   Holocene. Austrian J. Earth Sci. 102, 146–158.

886   Levenson, Y., Ryb, U., Emmanuel, S., 2017. Comparison of field and laboratory

887   weathering rates in carbonate rocks from an Eastern Mediterranean drainage

888   basin. Earth Planet. Sci. Lett. 465, 176–183.

889   https://doi.org/10.1016/j.epsl.2017.02.031

890   Loke, M.H., 2013. Tutorial : 2-D and 3-D electrical imaging surveys. Geotomo Softw.

891   Malaysia 127.

892   Loke, M.H., Acworth, I., Dahlin, T., 2003. A comparison of smooth and blocky

893   inversion methods in 2D electrical imaging surveys. Explor. Geophys. 34, 182–

894   187, pp. 128.

895 Machette, M.N., Slate, J.L., Phillips, F.M., 2008. Terrestrial Cosmogenic-Nuclide

896   Dating of Alluvial Fans in Death Valley, California. US Geol. Surv. Prof. Pap. 1–

897   54.

898 Marjanac, L., Marjanac, T., Mogut, K., 2001. Dolina Gumance u doba Pleistocena.

899   Zb. Društva za Povj. Klana 6, 321–330.

900 Marrero, S.M., Hein, A.S., Naylor, M., Attal, M., Shanks, R., Winter, K., Woodward,

901   J., Dunning, S., Westoby, M., Sugden, D., 2018. Controls on subaerial erosion

902   rates in Antarctica. Earth Planet. Sci. Lett. 501, 56–66.

903   https://doi.org/10.1016/J.EPSL.2018.08.018

904 Marrero, S.M., Phillips, F.M., Borchers, B., Lifton, N., Aumer, R., Balco, G., 2016a.

905   Cosmogenic nuclide systematics and the CRONUScalc program. Quat.

906   Geochronol. 31, 160–187. https://doi.org/10.1016/j.quageo.2015.09.005

907 Marrero, S.M., Phillips, F.M., Caffee, M.W., Gosse, J.C., 2016b. CRONUS-Earth

908   cosmogenic 36Cl calibration. Quat. Geochronol. 31, 199–219.

909   https://doi.org/10.1016/j.quageo.2015.10.002

910 Mechernich, S., Dunai, T.J., Binnie, S.A., Goral, T., Heinze, S., Dewald, A.,

911   Schimmelpfennig, I. Keddadouche, K., Aumaître, G., Bourlès, D., Marrero, S.,

912   Wilcken, K., Simon, K., Fink, D., Phillips, F.M., Caffee, M.W., Gregory, L.C.,

913   Phillips, R., Freemann, S.P.H.T., Shanks, R.P., Sarıkaya, M.A., Pavetich, S.,

914   Rugel, G., Merchel, S., Akçar, N., Yesilyurt, S., Ivy-Ochs, S. Vockenhuber, C.,

915   2019. Carbonate and silicate intercomparison materials for cosmogenic 36Cl

916   measurements. Nucl. Instruments Meas. Phys. Res. B.

917   Mechernich, S., Schneiderwind, S., Mason, J., Papanikolaou, I.D., Deligiannakis, G.,

918   Pallikarakis, A., Binnie, S.A., Dunai, T.J., Reicherter, K., 2018. The Seismic

919   History of the Pisia Fault (Eastern Corinth Rift, Greece) From Fault Plane

920   Weathering Features and Cosmogenic 36Cl Dating. J. Geophys. Res. Solid

921   Earth 123, 4266–4284. https://doi.org/10.1029/2017JB014600

922   Mercier, D., 2008. Paraglacial and paraperiglacial landsystems: concepts, temporal

923   scales and spatial distribution. Géomorphologie Reli. Process. Environ. 14,

924   223–233. https://doi.org/10.4000/geomorphologie.7396

925   Merritt, A.J., Chambers, J.E., Wilkinson, P.B., West, L.J., Murphy, W., Gunn, D.,

926   Uhlemann, S., 2016. Measurement and modelling of moisture-electrical

927   resistivity relationship of fine-grained unsaturated soils and electrical anisotropy.

928   J. Appl. Geophys. 124, 155–165. https://doi.org/10.1016/j.jappgeo.2015.11.005

929   Mihevc, A., Prelovšek, M., 2010. Geographical position and general overview, in:

930   Mihevc, A. (Ed.), Introduction to the Dinaric Karst. Karst Research Institute at

931   ZRC SAZU, Postojna, pp. S6-8.

932   Milivojević, M., Menković, L., Ćalić, J., 2008. Pleistocene glacial relief of the central

933   part of Mt. Prokletije (Albanian Alps). Quat. Int. 190, 112–122.

934   https://doi.org/10.1016/j.quaint.2008.04.006

935   Ministry of the Environment and Spatial Planning Slovenian Environment Agency,

936   n.d. LiDAR data Slovenia [WWW Document]. 2011. URL

937   http://gis.arso.gov.si/evode/profile.aspx?id=atlas_voda_Lidar@Arso

938 Monegato, G., 2012. Local glaciers in the Julian Prealps (NE Italy) during the Last

939   Glacial Maximum. Alp. Mediterr. Quat. 25, 5–14.

940 Moulin, A., Benedetti, L., Rizza, M., Jamšek Rupnik, P., Gosar, A., Bourlès, D.,

941   Keddadouche, K., Aumaître, G., Arnold, M., Guillou, V., Ritz, J.-F., 2016. The

942   Dinaric fault system: Large-scale structure, rates of slip, and Plio-Pleistocene

943   evolution of the transpressive northeastern boundary of the Adria microplate.

944   Tectonics 35, 2258–2292. https://doi.org/10.1002/2016TC004188

945 Oliva, M., Žebre, M., Guglielmin, M., Hughes, P.D., Çiner, A., Vieira, G., Bodin, X.,

946   Andrés, N., Colucci, R.R., García-Hernández, C., Mora, C., Nofre, J., Palacios,

947   D., Pérez-Alberti, A., Ribolini, A., Ruiz-Fernández, J., Sarıkaya, M.A., Serrano,

948   E., Urdea, P., Valcárcel, M., Woodward, J.C., Yıldırım, C., 2018. Permafrost

949   conditions in the Mediterranean region since the Last Glaciation. Earth-Science

950   Rev. 185, 397–436. https://doi.org/10.1016/j.earscirev.2018.06.018

951 Osmaston, H., 2005. Estimates of glacier equilibrium line altitudes by the

952   Area×Altitude, the Area×Altitude Balance Ratio and the Area×Altitude Balance

953   Index methods and their validation. Quat. Int. 138–139, 22–31.

954   https://doi.org/https://doi.org/10.1016/j.quaint.2005.02.004

955 Placer, L., 1998. Contribution to the macrotectonic subdivision of the border region

956   between Southern Alps and External Dinarides = Prispevek k makrotektonski

957   rajonizaciji mejnega ozemlja med Južnimi Alpami in Zunanjimi Dinaridi.

958   Geologija 41, 223–255.

959 Plan, L., 2005. Factors controlling carbonate dissolution rates quantified in a field test

960   in the Austrian alps. Geomorphology 68, 201–212.

961 https://doi.org/10.1016/J.GEOMORPH.2004.11.014

962 Pope, R.J., Hughes, P.D., Skourtsos, E., 2015. Glacial history of Mt Chelmos,

963 Peloponnesus, Greece. Geol. Soc. London, Spec. Publ. 433.

964 https://doi.org/10.1144/SP433.11

965 Pučnik, J., 1980. Velika knjiga o vremenu. Cankarjeva založba, Ljubljana.

966 Rea, B.R., 2009. Defining modern day Area-Altitude Balance Ratios (AABRs) and

967 their use in glacier-climate reconstructions. Quat. Sci. Rev. 28, 237–248.

968 https://doi.org/10.1016/J.QUASCIREV.2008.10.011

969 Reimer, P.J., Bard, E., Bayliss, A., Beck, J.W., Blackwell, P.G., Bronk Ramsey, C.,

970 Buck, C.E., Cheng, H., Edwards, R.L., Friedrich, M., Grootes, P.M., Guilderson,

971 T.P., Haflidason, H., Hajdas, I., Hatté, C., Heaton, T.J., Hoffmann, D.L., Hogg,

972 A.G., Hughen, K.A., Kaiser, K.F., Kromer, B., Manning, S.W., Niu, M., Reimer,

973 R.W., Richards, D.A., Scott, E.M., Southon, J.R., Staff, R.A., Turney, C.S.M.,

974 van der Plicht, J., 2013. IntCal13 and Marine13 Radiocarbon Age Calibration

975 Curves 0–50,000 Years cal BP. Radiocarbon 55, 1869–1887.

976 https://doi.org/10.2458/azu_js_rc.55.16947

977 Reynolds, J.M., 1997. An Introduction to Applied and Environmental Geophysics.

978 John Wiley & Sons Ltd, Chichester, UK.

979 Ribolini, A., Bini, M., Isola, I., Spagnolo, M., Zanchetta, G., Pellitero, R., Mechernich,

980 S., Gromig, R., Dunai, T., Wagner, B., Milevski, I., 2018. An Oldest Dryas glacier

981 expansion on Mount Pelister (Former Yugoslavian Republic of Macedonia)

982 according to 10Be cosmogenic dating. J. Geol. Soc. London. 175, 100–110.

983 https://doi.org/10.1144/jgs2017-038

984   Ribolini, A., Isola, I., Zanchetta, G., Bini, M., Sulpizio, R., 2011. Glacial features on

985   the Galicica Mountains, Macedonia: Preliminary report. Geogr. Fis. e Din. Quat.

986   34, 247–255. https://doi.org/10.4461/GFDQ.2011.34.22

987   Rixhon, G., May, S.M., Engel, M., Mechernich, S., Schroeder-Ritzrau, A., Frank, N.,

988   Fohlmeister, J., Boulvain, F., Dunai, T., Brückner, H., 2018. Multiple dating

989   approach (14C, 230Th/U and 36Cl) of tsunami-transported reef-top boulders on

990   Bonaire (Leeward Antilles) – Current achievements and challenges. Mar. Geol.

991   396, 100–113. https://doi.org/https://doi.org/10.1016/j.margeo.2017.03.007

992   Ruszkiczay-Rüdiger, Z., Braucher, R., Novothny, Á., Csillag, G., Fodor, L., Molnár,

993   G., Madarász, B., 2016a. Tectonic and climatic control on terrace formation:

994   Coupling in situ produced 10Be depth profiles and luminescence approach,

995   Danube River, Hungary, Central Europe. Quat. Sci. Rev. 131, 127–147.

996   https://doi.org/10.1016/J.QUASCIREV.2015.10.041

997   Ruszkiczay-Rüdiger, Z., Kern, Z., Urdea, P., Braucher, R., Madarász, B.,

998   Schimmelpfennig, I., 2016b. Revised deglaciation history of the Pietrele–

999   Stânişoara glacial complex, Retezat Mts, Southern Carpathians, Romania. Quat.

1000   Int. 415, 216–229. https://doi.org/10.1016/j.quaint.2015.10.085

1001   Ryb, U., Matmon, A., Erel, Y., Haviv, I., Katz, A., Starinsky, A., Angert, A., Team, A.,

1002   2014. Controls on denudation rates in tectonically stable Mediterranean

1003   carbonate terrain. GSA Bull. 126, 553–568.

1004   Schimmelpfennig, I., Benedetti, L., Finkel, R., Pik, R., Blard, P.-H., Bourlès, D.,

1005   Burnard, P., Williams, A., 2009. Sources of in-situ 36Cl in basaltic rocks.

1006   Implications for calibration of production rates. Quat. Geochronol. 4, 441–461.

1007 https://doi.org/https://doi.org/10.1016/j.quageo.2009.06.003

1008 Schmidt, S., Hetzel, R., Kuhlmann, J., Mingorance, F., Ramos, V.A., 2011. A note of

1009 caution on the use of boulders for exposure dating of depositional surfaces.

1010 Earth Planet. Sci. Lett. 302, 60–70. https://doi.org/10.1016/j.epsl.2010.11.039

1011 Šercelj, A., 1971. Postglacialni razvoj gorskih gozdov v severozahodni Jugoslaviji.

1012 Slovenska akademija znanosti in umetnosti, Ljubljana, pp. 30.

1013 Sharma, P., Kubik, P.W., Fehn, U., Gove, H.E., Nishiizumi, K., Elmore, D., 1990.

1014 Development of 36Cl standards for AMS. Nucl. Instruments Methods Phys. Res.

1015 Sect. B Beam Interact. with Mater. Atoms 52, 410–415.

1016 https://doi.org/10.1016/0168-583X(90)90447-3

1017 Siame, L., Bellier, O., Braucher, R., Sébrier, M., Cushing, M., Bourlès, D., Hamelin,

1018 B., Baroux, E., de Voogd, B., Raisbeck, G., Yiou, F., 2004. Local erosion rates

1019 versus active tectonics: cosmic ray exposure modelling in Provence (south-east

1020 France). Earth Planet. Sci. Lett. 220, 345–364. https://doi.org/10.1016/S0012-

1021 821X(04)00061-5

1022 Šifrer, M., 1959. Obseg pleistocenske poledenitve na Notranjskem Snežniku. Geogr.

1023 Zb. 5, 27–83.

1024 Šikić, D., Pleničar, M., Šparica, M., 1972. Osnovna geološka karta SFRJ. 1:100.000.

1025 List Ilirska Bistrica (Basic Geological Map of SFR Yugoslavia 1:100.000, Sheet

1026 Ilirska Bistrica). Zvezni geološki zavod, Beograd.

1027 Sarıkaya, M., Çiner, A., 2017. Late Quaternary glaciations in the eastern

1028 Mediterranean, in: Hughes, P., Woodward, J. (Eds.), Quaternary Glaciation in

1029   the Mediterranean Mountains. Geological Society of London Special Publication

1030   433, pp. 289–305. https://doi.org/10.1144/SP433.4

1031 Silvester, P.P., Ferrari, R.L., 1990. Finite elements for electrical engineers (2nd. ed.).

1032   Cambridge Univ. Press.

1033 Slaymaker, O., 2009. Proglacial, periglacial or paraglacial?, in: Knight, J., Harrison,

1034   S. (Eds.), Periglacial and Paraglacial Processes and Environments. The

1035   Geological Society of London, pp. 71–84.

1036 Smart, C., 2004. Glacierized and glaciated karst, in: Gunn, J. (Ed.), Encyclopedia of

1037   Caves and Karst Science. Fitzroy Dearborn, New York, pp. 804–809.

1038 Smart, P.L., 1986. Origin and development of glacio-karst closed depressions in the

1039   Picos de Europa, Spain. Zeitschrift für Geomorphol. 30, 423–443.

1040 Stone, J.O., 2000. Air pressure and cosmogenic isotope production. J. Geophys.

1041   Res. Solid Earth 105, 23753–23759. https://doi.org/10.1029/2000JB900181

1042 Stone, J.O., 2005. Terrestrial Chlorine-36 Production from Spallation of Iron, in: 10th

1043   AMS Conference. Berkeley.

1044 Stone, J.O., Allan, G.L., Fifield, L.K., Cresswell, R.G., 1996. Cosmogenic chlorine-36

1045   from calcium spallation. Geochim. Cosmochim. Acta 60, 679–692.

1046   https://doi.org/10.1016/0016-7037(95)00429-7

1047 Styllas, M.N., Schimmelpfennig, I., Benedetti, L., Ghilardi, M., Aumaître, G., Bourlès,

1048   D., Keddadouche, K., 2018. Late-glacial and Holocene history of the northeast

1049   Mediterranean mountain glaciers - New insights from in situ-produced 36Cl-

1050   based cosmic ray exposure dating of paleo-glacier deposits on Mount Olympus,

Greece. Quat. Sci. Rev. 193, 244–265.

https://doi.org/https://doi.org/10.1016/j.quascirev.2018.06.020

Surina, B., Wraber, T., 2005. Phytosociology and ecology of Carex mucronata on the Mt. Snežnik (SW Slovenia, Liburnian Karst). Wulfenia 12, 97–112.

Thomas, F., Godard, V., Bellier, O., Benedetti, L., Ollivier, V., Rizza, M., Guillou, V., Hollender, F., Aumaître, G., Bourlès, D.L., Keddadouche, K., 2018. Limited influence of climatic gradients on the denudation of a Mediterranean carbonate landscape. Geomorphology 316, 44–58. https://doi.org/10.1016/J.GEOMORPH.2018.04.014

Veress, M., 2017. Solution DOLINE development on GLACIOKARST in alpine and Dinaric areas. Earth-Science Rev. 173, 31–48. https://doi.org/10.1016/J.EARSCIREV.2017.08.006

Vrabec, M., Fodor, L., 2006. Late Cenozoic tectonics of Slovenia: structural styles at the Northeastern corner of the Adriatic microplate, in: Pinter, N., Grenerczy, G., Weber, J., Stein, S., Medak, D. (Eds.), The Adria Microplate: GPS Geodesy, Tectonics and Hazards, NATO Science Series. Springer, Dordrecht, pp. 151–168.

Woodward, J., Macklin, M., Hughes, P., Adamson, K.R., Lewin, J., 2014. The paraglacial concept revisited : the record from the Mediterranean mountains of Southern Europe, in: Geophysical Research Abstracts, Vol. 16, EGU2014-5517. p. 5517.

Zaninović, K., Gajić-Čapka, M., Perčec Tadić, M., Vučetić, M., Milković, J., Bajić, A., Cindrić, K., Cvitan, L., Katušin, Z., Kaučić, D., Likso, T., Lončar, Ž., Mihajlović,

1074   D., Pandžić, K., Patarčić, M., Srnec, L., Vučetić, V., 2008. Klimatski atlas

1075   Hrvatske / Climate atlas of Croatia 1961-1990., 1971-2000. Meteorological and

1076   Hydrological Service of Croatia, Zagreb.

1077   Žebre, M., 2015. Pleistocenska poledenitev obalnega dela Dinarskega gorstva

1078   (Pleistocene Glaciation of the Coastal Dinaric Mountains) (PhD thesis). Faculty

1079   of Arts, University of Ljubljana, Ljubljana, pp. 197.

1080   Žebre, M., Stepišnik, U., 2014. Reconstruction of Late Pleistocene glaciers on Mount

1081   Lovćen, Montenegro. Quat. Int. 353, 225–235.

1082   https://doi.org/10.1016/j.quaint.2014.05.006

1083   Žebre, M., Stepišnik, U., 2015. Glaciokarst landforms and processes of the southern

1084   Dinaric Alps. Earth Surf. Process. Landforms 40, 1493–1505.

1085   https://doi.org/10.1002/esp.3731

1086   Žebre, M., Stepišnik, U., 2016. Glaciokarst geomorphology of the Northern Dinaric

1087   Alps: Snežnik (Slovenia) and Gorski Kotar (Croatia). J. Maps 12, 873–881.

1088   https://doi.org/10.1080/17445647.2015.1095133

1089   Žebre, M., Stepišnik, U., Colucci, R.R., Forte, E., Monegato, G., 2016. Evolution of a

1090   karst polje influenced by glaciation: The Gomance piedmont polje (northern

1091   Dinaric Alps). Geomorphology 257, 143–154.

1092   https://doi.org/10.1016/j.geomorph.2016.01.005

1093   Žebre, M., Stepišnik, U., Kodelja, B., 2013. Traces of Pleistocene glaciation on

1094   Trnovski gozd | Sledovi pleistocenske Poledenitve na Trnovskem gozdu. Dela

1095   39, 157–170. https://doi.org/10.43121/dela.39.9.157-170

1096

1097 **Supplementary material**

Element	CRN PD-02/ 25-30	CRN PD-02/ 75-80	CRN PD-02/ 105-110	Average
Fusion inductively coupled plasma (FUS-ICP AES)				
SiO_2	4,73%	0,71%	0,75%	2,06%
Al_2O_3	0,31%	0,13%	0,19%	0,21%
Fe_2O_3	0,21%	0,10%	0,12%	0,14%
MnO	0,007%	0,004%	0,003%	0,005%
MgO	1,70%	1,24%	1,39%	1,44%
CaO	51,3%	53,8%	54,6%	53,2%
Na_2O	0,0007	0,03%	0,07%	0,06%
K_2O	0,06%	0,02%	0,04%	0,04%
TiO_2	0,027%	0,007%	0,004%	0,013%
P_2O_5	< 0.01 %	0,01%	0,01%	0,01%
CO_2 (LOI)	40,6%	42,7%	42,4%	41,9%
Total	99,0%	98,7%	99,51%	99,07%
Gravimetric				
H_2O	0,3%	0,3%	0,2%	0,27%
Fusion mass spectrometry (FUS-ICP MS)				
Rb	< 2 µg/g	< 2 µg/g	< 2 µg/g	0 µg/g
Sm	0.5 µg/g	< 0.1 µg/g	< 0.1 µg/g	0.2 µg/g
Gd	0.6 µg/g	0.1 µg/g	< 0.1 µg/g	0.2 µg/g
Th	0.2 µg/g	< 0.1 µg/g	< 0.1 µg/g	0.1 µg/g
U	1.5 µg/g	2.2 µg/g	3.1 µg/g	2.3 µg/g
Fusion inductively coupled plasma (FUS-ICP AES)				
Ba	12 µg/g	6 µg/g	6 µg/g	
Sr	190 µg/g	254 µg/g	227 µg/g	224 µg/g
Zr	10 µg/g	3 µg/g	4 µg/g	5.67 µg/g
Total digestion inductively coupled plasma (TD-ICP)				
Li	1 µg/g	< 1 µg/g	< 1 µg/g	0.3 µg/g
Prompt gamma neutron activation analysis (PGNAA)				
B	< 0.5 µg/g	< 0.5 µg/g	7.3 µg/g	2.5 µg/g
Accelerator Mass Spectroscopy (AMS; Table S1)				
Cl	47.3 µg/g	48.5 µg/g	49.7 µg/g	49.6 µg/g

1098

1099 **Table S1.** Relevant chemical composition of untreated samples measured at

1100 Activation laboratories (Canada) and by AMS (accelerator mass spectrometry;

1101 measurements in this study). Values below detection limit are marked with "<". LOI:

1102   loss on ignition. The average composition of the three samples was used for the

1103   depth profile modelling.

Sample ID [a]	Sample weight	Spike weight [b]	$^{36}Cl/^{35}Cl$ [c] (-)	$\pm\,^{36}Cl/^{35}Cl$ (-)	$^{36}Cl/^{37}Cl$ [c] (-)	$\pm\,^{36}Cl/^{37}Cl$ (-)	$^{35}Cl/^{37}Cl$ [c] (-)	$\pm\,^{35}Cl/^{37}Cl$ (-)	^{36}Cl conc. (atoms g^{-1})	$\pm^{36}Cl$ conc. (atoms g^{-1})	$\pm^{36}Cl$ conc. (%)	Cl $_{nat}$ AMS (µg/g)	$\pm$Cl $_{nat}$ AMS (µg/g)	blank correction (%)	^{36}Cl total prod. rate [d] (atoms/g/yr)	^{36}Cl prod. by neutrons [d] (atoms/g/yr)	^{36}Cl prod. thermal neutrons [d] (atoms/g/yr)	^{36}Cl prod. by muons [d] (atoms/g/yr)
CRN PD-02/25-30	20,1379	1,4848	2,81E-13	1,18E-14	1,98E-12	8,29E-14	7,05	0,04	5,11E+05	2,26E+04	4,4%	47,3	1,9	0,41%	41,23	26,09	9,33	4,83
CRN PD-02/75-80	20,4658	1,4892	1,73E-13	8,17E-15	1,20E-12	5,67E-14	6,94	0,04	3,14E+05	1,56E+04	5,0%	48,5	2,0	0,66%	24,37	13,15	6,17	4,51
CRN PD-02/ 105-110	19,7269	1,4859	1,39E-13	5,71E-15	9,71E-13	3,98E-14	6,97	0,04	2,61E+05	1,14E+04	4,4%	49,7	2,0	0,82%	17,76	8,71	4,34	4,33
CRN PD-02/ 215-220	29,6144	1,4832	2,02E-13	7,29E-15	1,19E-12	4,31E-14	5,91	0,04	2,95E+05	1,21E+04	4,1%	49,6	2,2	0,48%	7,15	1,93	1,36	3,71
Blank B17/05	-	1,3861	1,85E-15	4,51E-16	3,48E-14	8,47E-15	18,78	0,11	-	-	-	-	-	-	-	-	-	-
CoCal-N_UEdin-CologneAMS-1	8,4195	1,1907	1,55E-12	4,18E-14	2,86E-11	7,73E-13	18,48	0,31	3,62E+06	9,95E+04	2,7%	1,3	0,9	0,35%	-	-	-	-
CoCal-N_UEdin-CologneAMS-2	8,6312	1,1891	1,64E-12	4,45E-14	3,04E-11	8,25E-13	18,56	0,31	3,74E+06	1,03E+05	2,8%	1,1	0,8	0,33%	-	-	-	-
CoCal-N_UEdin-CologneAMS-3	8,7859	1,1880	1,65E-12	4,76E-14	3,08E-11	8,86E-13	18,63	0,31	3,69E+06	1,08E+05	2,9%	1,0	0,8	0,33%				
CoCal-N_UEdin-CologneAMS-4	8,3094	1,1940	1,56E-12	4,37E-14	2,89E-11	8,09E-13	18,51	0,31	3,71E+06	1,05E+05	2,8%	1,3	0,9	0,34%	-	-	-	-
CoCal-N_UEdin-CologneAMS-5	5,8187	1,1901	1,09E-12	3,75E-14	2,05E-11	7,05E-13	18,98	0,32	3,64E+06	1,28E+05	3,5%	0,5	1,2	0,50%	-	-	-	-
CoCal-N_UEdin-CologneAMS-6	5,6722	0,8387	1,53E-12	4,47E-14	2,82E-11	8,24E-13	18,46	0,31	3,74E+06	1,11E+05	3,0%	0,8	1,1	0,50%	-	-	-	-
CoCal-N_UEdin-CologneAMS-7	5,7713	1,1923	1,09E-12	3,35E-14	2,02E-11	6,22E-13	18,61	0,31	3,71E+06	1,16E+05	3,1%	1,6	1,3	0,50%	-	-	-	-
CoCal-N_UEdin-CologneAMS-8	5,5543	1,1874	1,03E-12	2,95E-14	1,90E-11	5,47E-13	18,53	0,31	3,62E+06	1,06E+05	2,9%	1,9	1,3	0,53%	-	-	-	-
CoCal-N_UEdin-CologneAMS-9	11,2870	1,1896	2,13E-12	5,96E-14	3,97E-11	1,11E-12	18,67	0,31	3,71E+06	1,05E+05	2,8%	0,7	0,6	0,25%	-	-	-	-
Blank-CoCal-Uedin	-	1,1863	5,49E-15	1,53E-15	1,04E-13	2,90E-14	19,16	0,32	-	-	-	-	-	-	-	-	-	-

[a] The CoCal-N intercomparison material yields an initial consensus value of (3.74 ± 0.10) x 10^6 at ^{36}Cl/g and 0.73 ± 0.18 µg/g of natural chlorine (Mechernich et al., 2019).

[b] Chlorine mass of $^{35}Cl/^{37}Cl$ spike added to the sample prior to dissolution. Spike concentration: mg Cl/g solution = 5.4569, $^{35}Cl/^{37}Cl$ = 19.960.

[c] The AMS machines were calibrated and normalized to three different concentrated standards ($^{36}Cl/Cl$: 5.000 × 10^{-13}, 1.600 × 10^{-12}, and 1.000 × 10^{-11}) from the NIST SRM 4943 material (Sharma et al., 1990).

[d] All given production rates account for the case of no erosion.

Table S2. ^{36}Cl sample preparation details and resulting Cl AMS ratios, ^{36}Cl and natural chlorine concentrations, and the sample-specific ^{36}Cl production rates. All errors are given as 1σ uncertainties.